Research Square

Preprints are preliminary reports that have not undergone peer review.
They should not be considered conclusive, used to inform clinical practice,
or referenced by the media as validated information.

Spatiotemporal Characteristics of the Atmospheric Boundary Layer Height over India Deduced from Multi-platform Measurements and Re-analyses Data

Srinivasan Prasanth

prasanthphy57@gmail.com

Indian Institute of Science Bangalore

Balachandran Gayathri

Indian Institute of Science Bangalore

Research Article

Keywords: Atmospheric boundary layer height, IMDAA, Characterization, Validation, Indian region

Posted Date: March 16th, 2026

DOI: https://doi.org/10.21203/rs.3.rs-8584444/v1

License: This work is licensed under a Creative Commons Attribution 4.0 International License.
Read Full License

Additional Declarations: No competing interests reported.

Version of Record: A version of this preprint was published at Meteorology and Atmospheric Physics on September 2nd, 2026. See the published version at https://doi.org/10.1007/s00703-026-01202-2.

Spatiotemporal Characteristics of the Atmospheric Boundary Layer Height over India Deduced from Multi-platform Measurements and Re-analyses Data

Srinivasan Prasanth[1]*, Balachandran Gayathri[1]

Divecha Centre for Climate Change, Indian Institute of Science, Bengaluru, India

*Corresponding author: Srinivasan Prasanth (prasanthphy57@gmail.com; prasanths@iisc.ac.in)

ORCID:

Srinivasan Prasanth: 0000-0001-6208-1334

Balachandran Gayathri: 0000-0003-4141-267X

Abstract

Atmospheric Boundary Layer Height (Z_i), a key characteristic of the boundary layer, is a crucial parameter in modelling cloud formation, weather, and air quality. Hence, its accuracy is vital for reliable modelling and forecasting. In this study, India's first regional reanalysis dataset, the Indian Monsoon Data Assimilation and Analysis (IMDAA), is validated against multi-platform measurement datasets. It is found that Z_i from IMDAA is in good agreement with radiosonde and satellite observations and performs better than the other reanalysis datasets. However, IMDAA significantly underestimates Z_i (<100 m) during December over humid subtropical climatic regions like Jammu and Gorakhpur, possibly due to high negative net radiation, overestimated cloud cover, and inaccuracies in surface energy partitioning in the IMDAA. For the first time, a comprehensive characterization of the daily maximum Z_i (referred to as $Z_{i,max}$) is performed. The analysis of diurnal and seasonal variations of $Z_{i,max}$ revealed that the atmospheric boundary layer is fully developed (deepest) at ~15:30 IST across all seasons over most of the Indian region. Spatially, $Z_{i,max}$ reached its highest value of ~4500 m during the pre-monsoon season over central India. But during the monsoon, it reduces to ~2500 m, and the peak location gets shifted to northwest India. In addition, we report that it is the sensible heat flux that primarily drives the $Z_{i,max}$ rather than the Bowen ratio over central India. These results have large implications for Z_i dynamics in regional numerical weather, climate, and air quality simulations.

Keywords: Atmospheric boundary layer height, IMDAA, Characterization, Validation, Indian region

1. Introduction

Atmospheric Boundary Layer (ABL), the lowest layer of the troposphere, is directly coupled with the Earth's surface through convective heat transfer, frictional drag, evaporation, and flow modification by topography (Stull, 1988). Hence, it plays a paramount role in modulating cloud formation, air pollution (dispersion), and regional weather in the lower troposphere (Stull, 1988; Garratt, 1994b; Oke, 2002). The height of the ABL (hereafter referred to as 'Z_i') is widely used to characterize the vertical mixing of aerosols/trace gases, heat, and moisture within this layer and the exchange of these quantities between the ABL and free troposphere (Bhumralkar, 1976; Seibert et al., 2000). It exhibits spatial and temporal variation across the globe, ranging from a few hundred meters to a few kilometers (Stull, 1988), and is crucial for a realistic simulation of vertical mixing, weather, and the forecast of air quality. An accurate estimate of Z_i can be made from various ground-based measurements, such as

radiosonde (Hennemuth and Lammert, 2006), lidar (Russell et al., 1974; Hennemuth and Lammert, 2006), SODAR (Beyrich, 1997), wind profiler (Bianco and Wilczak, 2002), ceilometer (Eresmaa et al., 2006), microwave radiometer (Min et al., 2020), and also using space-borne instruments (Kursinski et al., 1997; Basha and Ratnam, 2009). Despite being accurate, these measurements are highly limited in space and time and act as point measurements. For regional and global modelling applications, Z_i is also provided by several reanalysis products at high spatial and temporal resolution (Kanamitsu et al., 2002; Dee et al., 2011; Rienecker et al., 2011; Kobayashi et al., 2015; Kalnay et al., 2018; Laloyaux et al., 2018; Hersbach et al., 2020). Even though the reanalysis-based Z_i is reasonably accurate in some regions (Guo et al., 2016; Li et al., 2023; Wang et al., 2023; Xu et al., 2023), it also carries large uncertainty over several other regions, such as the Western hemisphere, Africa, the United States, Europe, Central Amazonia, and Asia (Jordan et al., 2010; Seidel et al., 2012; Si et al., 2018; Y. Zhang et al., 2020; Dias-Júnior et al., 2022). The uncertainty in Z_i results in unrealistic atmospheric modeling outputs such as surface level black carbon, particulate matter 2.5, turbulent vertical mixing, and precipitation etc (Moorthy et al., 2013; Govardhan et al., 2015; Gunwani et al., 2023).

For this reason, several efforts have been made to evaluate the performance of Z_i from various reanalysis products across different regions (with measurements): ECMWF (European Centre for Medium-Range Weather Forecasts) forecasts over oceanic regions (Lavers et al., 2019); ERA5 (ECMWF Reanalysis version 5) over Arctic, central Amazonia, contiguous United States, China, Tibetan Plateau, Gurbantünggüt Desert (Zhang et al., 2020; Dias-Júnior et al., 2022; Slättberg et al., 2022; Li et al., 2023; Wang et al., 2023; Xu et al., 2023; Xi et al., 2024); MERRA (Modern-Era Retrospective analysis for Research and Applications) over Western Hemisphere and Africa (Jordan et al., 2010); ERA-interim over China (Guo et al., 2016); MERRA-2, JRA-55 (Japanese 55-year Reanalysis) and NCEP-FNL (National Centers for Environmental Prediction final operational data) over Gurbantünggüt Desert and China (Wang et al., 2023; Xu et al., 2023); CERA (coupled ECMWF atmospheric reanalysis of medium-range weather) (Xu et al., 2023).

A few studies have evaluated the reanalysis-based Z_i and characterized it over the Indian region as well (Sathyanadh et al., 2017; Budakoti and Singh, 2021; Saha et al., 2022; Gogoi et al., 2024; Kundan et al., 2024; Shukla et al., 2024). Recently, Shukla et al. (2024) compared the Z_i from IMDAA (Indian Monsoon Data Assimilation and Analysis), India's first regional reanalysis dataset, with those obtained from ERA5, and MERRA-2, and studied the climatology of mean IMDAA Z_i over the Indian region. However, it did not attempt a validation against values derived from experimental measurements. Furthermore, previous studies focused on understanding variabilities of mean Z_i, but the daily $Z_{i,max}$ (i.e., the deepest Z_i observed in each day) is a more relevant parameter in weather and air pollution forecast, as it modulates the extent of convective mixing and pollutant dispersion (Lieman and Alpert, 1993; Zilitinkevich et al., 2012; Qu et al., 2017). In addition, the $Z_{i,max}$ represents a fully developed ABL and better captures turbulence and extreme boundary layer conditions than the mean Z_i. Despite its significance, the variability and characteristics of the $Z_{i,\,max}$ over the Indian region have not been studied in detail except by Sathyanadh et al. (2017), who carried out an analysis using the MERRA-2 dataset. However, recently, Shukla et al. (2024) have shown that MERRA-2 overestimates the Z_i over the Indian region. This scenario calls for a focused and systematic analysis aiming to study the characteristics and examine the variabilities of the $Z_{i,max}$ using a better dataset like the IMDAA reanalysis, a state-of-the-art high-resolution regional reanalysis product specifically designed for the Indian subcontinent (Rani et al., 2021).

In the above backdrop, this study aims to validate IMDAA Z_i using multi-platform observations such as GPS radiosonde and COSMIC-RO, as well as against the ERA model to determine its reliability and potential advantages (or limitations) over the existing datasets. Followed by this, we explore the diurnal and seasonal variability of $Z_{i,max}$, and characterize it over the Indian region using the IMDAA reanalysis product.

In the following sections, we first describe the data and methodology used in this study in Section 2. The cross-validation of Z_i from multi-platform observation is given in Section 3.1, characterization of the diurnal and seasonal variation of IMDAA $Z_{i,max}$ is given in Section 3.2, and the study is concluded in Section 4.

2 Data and methodology

2.1 Balloon-borne Observations

The National Atmospheric Research Laboratory (NARL) provides daily GPS radiosonde profiles at a vertical resolution of ~5 m at 17:30 IST for Gadanki (13.5ºN, 79.2ºE, altitude of 370 m above mean sea level). For the present study, the radiosonde observations from 2008 to 2018 are used. In addition, the University of Wyoming provides GPS radiosonde measurements with a vertical resolution of 50 m to 150 m for several stations across the globe daily at 05:30 IST and 17:30 IST (https://weather.uwyo.edu/upperair/sounding.html). From this, we have chosen nine inland stations spread across the Indian region, namely Jammu, New Delhi, Jodhpur, Gorakhpur, Ahmedabad, Nagpur, and Bengaluru for the year 2018 at 17:30 IST, and the locations of these stations are shown in Fig. 1.

Compared to the Wyoming GPS radiosonde, the NARL GPS radiosonde has a high vertical resolution, which makes it suitable for cross-validation of estimated Z_i from various satellite-based and reanalysis-based Z_i. But the Wyoming GPS radiosonde has better spatial coverage, making it suitable to evaluate the IMDAA Z_i over the Indian region.

2.2 Space-borne Observations

Constellation Observing System for Meteorology, Ionosphere, and Climate Global Positioning System Radio Occultation (COSMIC GPS-RO) is a constellation of six satellites which was launched in April 2006 and provides ~1500 high-resolution atmospheric refractivity profiles per day across the globe (http://cosmicio.cosmic.ucar.edu/cdaac/; Kursinski et al., 1997; Chan and Wood, 2013). The availability of the COSMIC-RO refractivity profile at a certain location is subject to the occurrence of occultation over the location. Hence, the COSMIC-RO profiles are non-gridded and highly sparse in space and time. In the present study, COSMIC-RO refractivity profiles within a 3° × 3° grid, centered around the ground station, and coinciding with NARL Gadanki radiosonde measurements with a time window of 17:30 ± 3 hours from 2008 to 2018, are selected. Profiles with the quality flag of '0' (i.e., bad quality) and profiles which did not reach at least 3 km above the ground level are screened out (Singh et al., 2021). Out of the screened profiles, 26 high-quality profiles showing a sharp vertical gradient are considered for cross-validation purposes.

2.3 Reanalysis Dataset

The Indian Monsoon Data Assimilation and Analysis (IMDAA) is India's first regional reanalysis data (Rani et al., 2021), generated by the National Centre for Medium-Range Weather Forecasting (NCMRWF) in collaboration with the India Meteorological Department (IMD) and the United Kingdom Met Office (https://rds.ncmrwf.gov.in/). It provides high-resolution regional reanalysis data over the Indian (South Asian) region (30° E to 120° E, and 15° S to 45° N) at a horizontal resolution of ~12 km (~0.11° × 0.11°) and a temporal resolution of 1 hour, with 63 vertical levels up to an altitude of ~40 km, for the period 1979 to 2024. The dataset is based on a four-dimensional variational assimilation scheme (4D-VAR) where observations from various platforms, such as aircraft, radiosonde, surface, etc., are assimilated (Rani et al., 2021). For the present study, IMDAA (version 3) hourly mean Z_i from 2008 to 2018 is utilized.

ERA5 is a global reanalysis dataset from ECMWF, which provides numerous meteorological and atmospheric parameters (https://cds.climate.copernicus.eu/; Hersbach et al., 2020). The ERA5 product provides Z_i with a horizontal resolution of 0.25° × 0.25°, and a temporal resolution of 1 hour, at 37 pressure levels from 1000 hPa to 1 hPa (Zhang et al., 2020). For the present study, ERA5 is used during the same period as that of IMDAA.

2.4 Study Region

The present study is focused on the Indian region and covers four distinct seasons: Winter (December, January, and February), Pre-monsoon (March, April, and May), Monsoon (June, July, August, and September), and Post-monsoon (October and November). The study region, along with locations of the radiosonde stations from Wyoming (red circles) and NARL (blue diamond), is shown in Fig. 1.

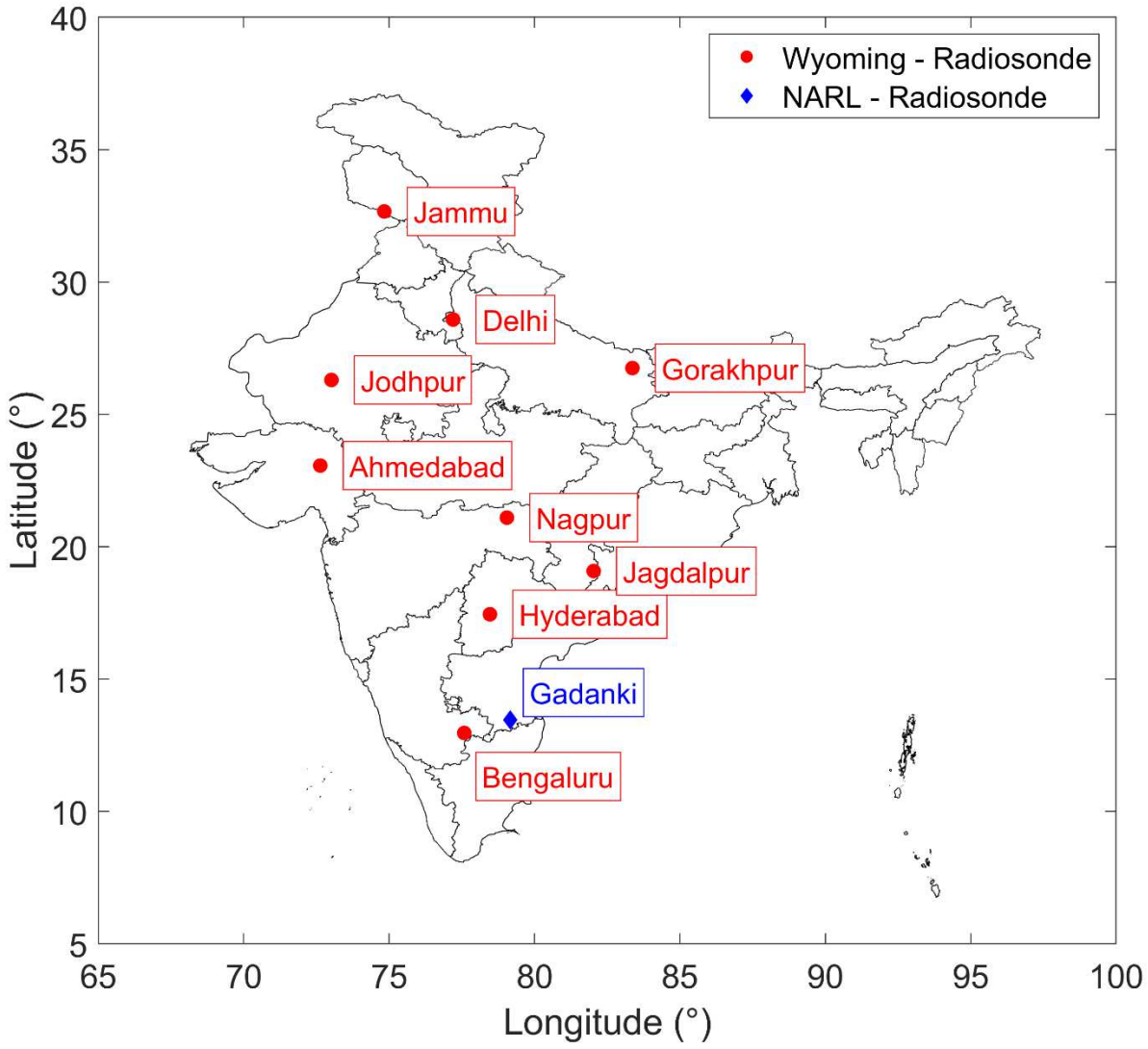


Fig. 1 *Geographical map showing the study region. The filled red circles mark the location of Wyoming radiosonde stations, and the blue diamond marks the GPS radiosonde station*

2.5 Methodology

The vertical gradient of the thermodynamic variables is often used to estimate Z_i (Heffter J. L., 1980; Van Ulden and Holtslag, 1985; Holtslag et al., 1995). In the present study, four thermodynamic variables, such as potential temperature (θ), virtual potential temperature (θ_v), mixing ratio (r), and refractivity (N), are used. The refractivity profiles are derived following Smith and Weintraub (1953) as:

$$N = 77.6 \times \frac{P}{T} + 3.73 \times 10^5 \times \frac{e}{T^2} \qquad (1)$$

where P is the atmospheric pressure in hPa, T is the atmospheric temperature in Kelvin, N is the refractivity, and e is the water vapor partial pressure in hPa.

Altitude at which the maximum gradient of θ, θ_v, and the minimum gradient of r and N is considered as the Z_i (Basha and Ratnam, 2009; Seidel et al., 2010). Following this, any three gradient methods yielding the same Z_i value are considered as the final Z_i.

To understand the variability of the boundary layer, key factors such as Bowen ratio (B), wind shear (S), Monin-Obukhov stability parameter (ζ), and water vapor pressure deficit (VPD) are used, and they are estimated (Stull, 1988) as:

$$B = \frac{H}{LE} \tag{2}$$

$$S = \frac{1}{\Delta z}\sqrt{\left(u_{z_{50}} - u_{z_{10}}\right)^2 + \left(v_{z_{50}} - v_{z_{10}}\right)^2} \tag{3}$$

$$\zeta = \frac{z}{L} \tag{4}$$

$$L = -\frac{u_*^3 T_{z_2}}{kg(\frac{H}{\rho c_p})} \tag{5}$$

$$u^* = \frac{(kU_{z_{10}})}{\log(\frac{z}{z_0})} \tag{6}$$

$$VPD = 0.6108 \times e^{(\frac{17.27 \times T_{z_2}}{T_{z_2}+237.3})} \times (1 - \frac{RH_{z_2}}{100}) \tag{7}$$

where H is sensible heat flux (W m^{-2}), LE is latent heat flux (W m^{-2}), $u_{z_{50}}$ and $v_{z_{50}}$ are zonal and meridional wind velocity (m s^{-1}) at the height of 50 m, respectively, and $u_{z_{10}}$ and $v_{z_{10}}$ are zonal and meridional wind velocity (m s^{-1}) at the height of 10 m, respectively, and Δz is 40 m. z is the measurement height above the surface (in this case, 10 m), L is Monin-Obukhov length (m), u* is friction velocity (m s^{-1}), T_{z_2} is temperature at 2 m above surface (K), k is von Kármán constant (taken as 0.4), g is acceleration due to gravity (9.8 m s^{-2}), ρ is air density (kg m^{-3}), c_p is specific heat capacity of air at constant pressure (1004 J kg^{-1} K^{-1}), $U_{z_{10}}$ is the mean velocity at 10 m above the surface (m s^{-1}), z_0 is surface roughness length (m), and RH_{z_2} is relative humidity at 2 m above the surface (%). It is important to note that all the above equations use IMDAA data. While estimating the Monin-Obukhov length (L) through Eq. (5), the temperature at 2 m above the surface is used instead of the 10 m value, as the IMDAA dataset does not provide temperature at 10 m. The potential error introduced by this substitution is assumed to be negligible.

The Bowen ratio indicates how the available surface energy is partitioned between sensible and latent heat flux (Stull, 1988); B > 1 suggests that the sensible heat dominates over latent heat and contributes to heating the layer above the surface and promotes the boundary layer growth and B < 1 suggests that the latent heat dominates over the sensible heat and convection is not promoted and thus growth of the boundary layer is suppressed. Whereas B ≈ 1 indicates that the sensible and latent heat are almost equal. The Monin-Obukhov stability parameter is useful in understanding the atmospheric stability (Stull, 1988): When ζ < -0.1, the atmosphere is unstable, meaning surface heating dominates and buoyant (thermal) turbulence is strong (Högström, 1988). When $-0.1 \leq \zeta \leq 0.1$, the atmosphere is neutral, where turbulence is primarily generated by mechanical shear, and buoyancy has little effect.

When $\zeta > 0.1$, the atmosphere is stable, meaning surface cooling dominates, and buoyancy suppresses turbulence, leading to weaker mixing. In addition, the net radiation (R_{net}) is estimated as follows:

$$R_{net} = S_d - S_u + L_d - L_u \quad (8)$$

Here, R_{net} governs the overall energy available for surface heating and thus influences the depth of the ABL; higher R_{net} generally leads to a deeper ABL due to increased turbulent mixing. S_d, the downward shortwave radiation, represents incoming solar energy reaching the surface. It increases and promotes surface heating, promotes turbulence, and deepens the boundary layer. S_u, the upward shortwave radiation, is the portion of solar radiation reflected by the surface and is strongly influenced by surface albedo, such that higher S_u (from high-albedo surfaces) reduces net surface heating and thus limits boundary layer growth. During nighttime or under cloudy conditions, longwave processes dominate. L_u, the upward longwave radiation, is emitted by the Earth's surface and contributes to radiative cooling, stabilizing the near-surface layer and suppressing vertical mixing. L_d , the downward longwave radiation, typically emitted by clouds and atmospheric water vapor, acts to reduce surface cooling by delivering energy downward, thereby slowing or reducing the stabilization of the boundary layer.

3. Results and discussion

3.1 Cross-validation of Z_i from multiplatform observations

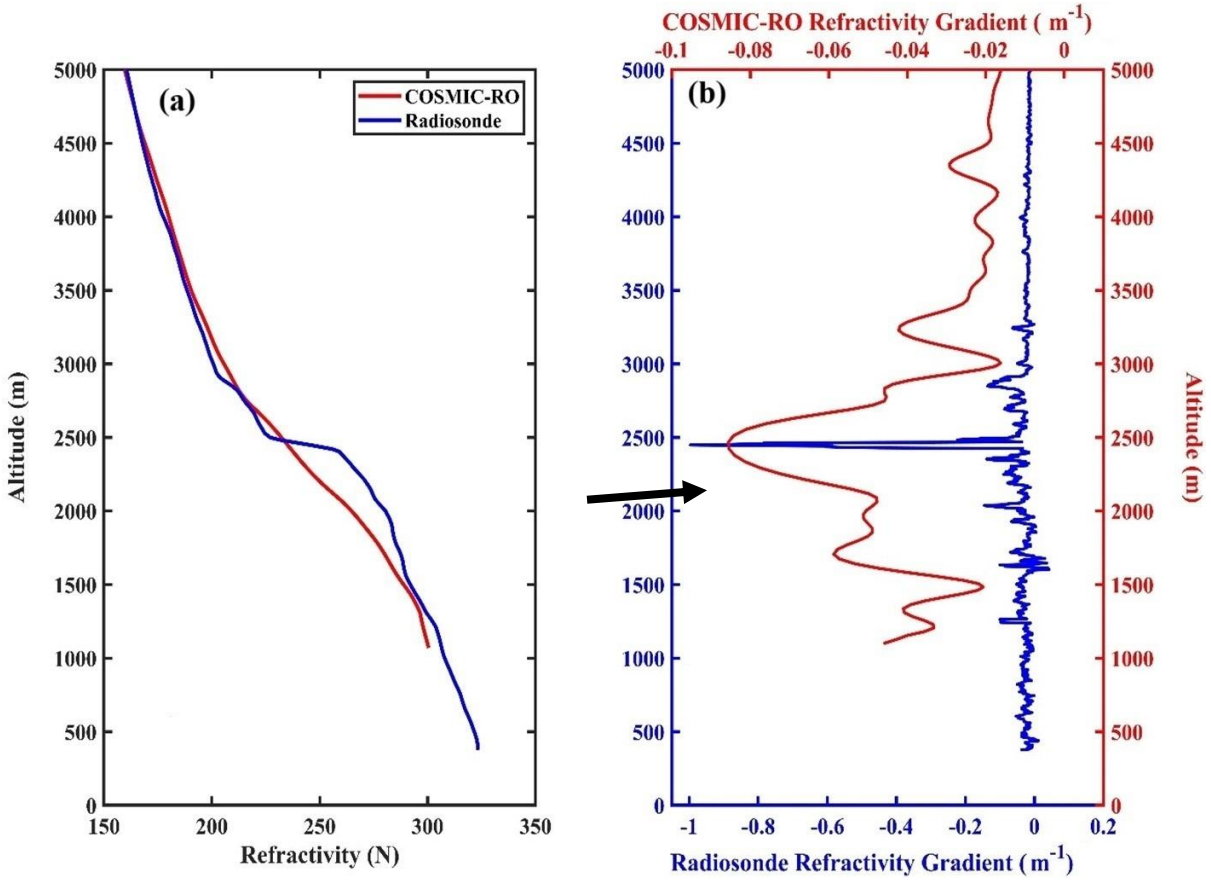


Fig. 2 *Panel (a) shows the refractivity profiles from GPS radiosonde and COSMIC-RO for a representative day (15-02-2018) at 17:30 IST, and panel (b) shows the corresponding gradients. The black arrow marks the altitude of the lowest value of the gradients (~2500 m), indicating the* Z_i

The COSMIC-RO provides high-resolution refractivity profiles, which are useful in estimating Z_i with high accuracy, showing mean relative deviations of less than 0.5% compared to radiosonde observations up to 30 km altitude (Xu et al., 2009; Guo et al., 2011). The refractivity profiles derived from the GPS radiosonde (estimated using Eq. 1 in Section 2.5) and the COSMIC-RO measurements over the Gadanki region exhibit good overall consistency. Fig. 2a presents a representative case observed on 15 February 2018 at 17:30 IST, where both profiles show a coinciding peak in the negative gradient, yielding a comparable Z_i value of approximately 2500 m (indicated by a black arrow in Fig. 2b), thereby demonstrating their close agreement. To cross-validate the Z_i from various sources, such as COSMIC-RO, GPS radiosonde (from NARL), IMDAA, and ERA5, coincident profiles over Gadanki from 2008 to 2018 are chosen. We limit the cross-validation to the Gadanki region due to the availability of high-resolution GPS radiosonde measurements (~5 m), which ensures the best data set to estimate Z_i. Following the rigorous screening procedures for the COSMIC-RO profiles described in Section 2.2, a total of 26 high-quality COSMIC-RO profiles were retained, excluding those that did not extend to at least 3 km altitude. Although the analysis covers 10 years, the number of available profiles is limited because COSMIC overpasses over the region are infrequent, and many profiles fail to meet the required vertical coverage and quality criteria. The corresponding ERA5 and IMDAA datasets were subsequently employed for cross-validation.

The gradient technique is extended to all chosen profiles, and Z_i is estimated. A cross-validation of Z_i was conducted using linear regression analysis to evaluate the consistency among different datasets. Specifically, the radiosonde Z_i was compared with Z_i values from COSMIC-RO, ERA5, and IMDAA reanalysis data. Additionally, a direct comparison was performed between IMDAA Z_i and COSMIC-RO Z_i to assess their mutual agreement. This approach helps to identify the reliability and potential biases of reanalysis-derived Z_i against observational Z_i. The validation results are shown using scatter plots in Fig. 3.

Based on the statistical analysis of Z_i comparisons shown in Fig. 3, it is evident that the IMDAA exhibits a stronger agreement with radiosonde observations than ERA5 and even COSMIC-RO. The linear regression between IMDAA and radiosonde Z_i (Fig. 3b) yields a correlation coefficient (R) of 0.77, notably higher than the weak correlation of 0.31 seen with ERA5 (Fig. 3c), indicating that ERA5 substantially underrepresents Z_i variability. Although COSMIC-RO shows the highest correlation with radiosonde (R = 0.94; Fig. 3a), it overestimates Z_i at higher values, as evidenced by the slope exceeding 1 (1.19) and a large negative intercept of -719.71. In contrast, the regression line (slope = 0.92, intercept = –491.89) between the IMDAA and radiosonde is closer to the 1:1 relationship, suggesting a more consistent and less biased estimation across the range (Fig. 3b). Furthermore, the comparison between IMDAA and COSMIC-RO (R = 0.76; Fig. 3d) reinforces IMDAA's robustness in capturing Z_i. Overall, these results underscore that IMDAA provides the most balanced and statistically reliable representation of Z_i among the datasets cross-validated at the Gadanki region.

Having established the reliability of IMDAA Z_i through cross-validation, we now proceed with a more in-depth analysis of its consistency across India, covering various geographical regions and conditions. For this purpose, the validation is extended to include nine additional radiosonde stations from the Wyoming sounding network across India.

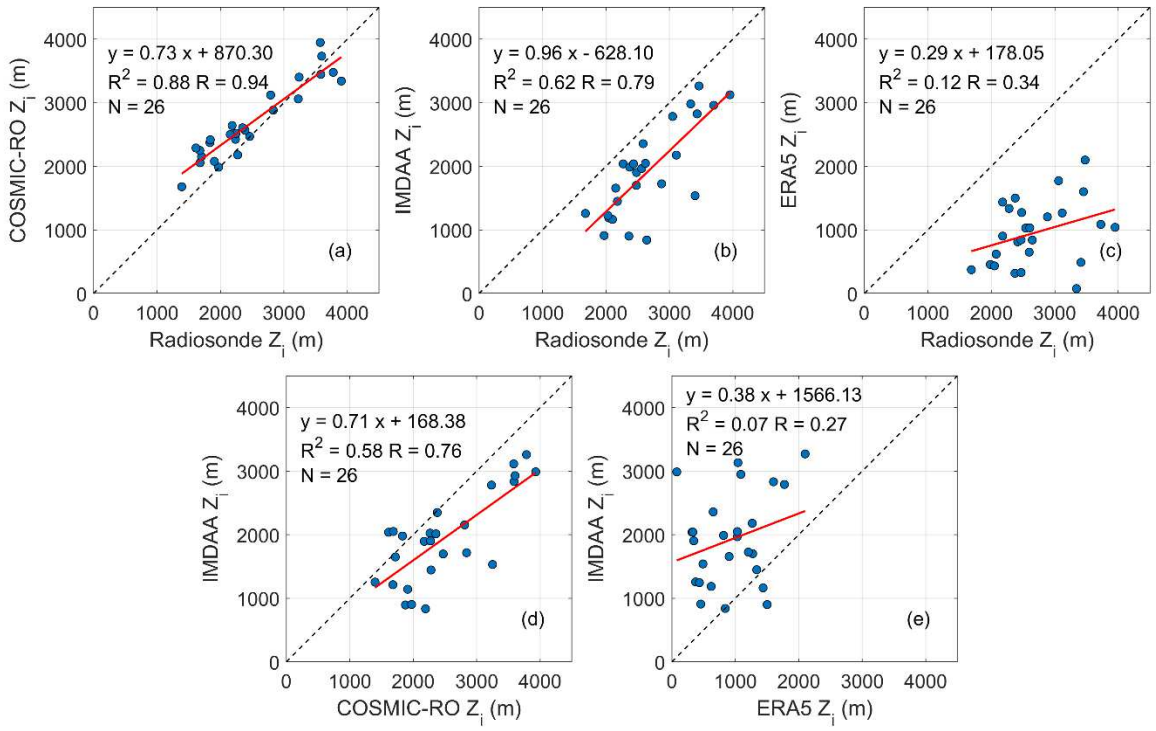


Fig. 3 *Cross-validation of the Z_i from multi-platform measurements. The blue circle indicates the Z_i data, the red solid line indicates the least square linear regression fit, and the dashed line represents 1:1. Here, 'R' is the correlation coefficient, 'R^2' is the coefficient of determination, and 'N' is the total number of points used for regression*

3.2 Evaluation of the IMDAA Z_i across the Indian region

The Wyoming radiosonde stations provide the balloon-borne atmospheric observations such as pressure, temperature, water mixing ratio, etc. The Z_i from the Wyoming radiosonde station is estimated using the integrated gradient technique described in Section 2.5. A representative of Z_i estimation from the radiosonde profile from Nagpur, measured on 17-01-2018 at 17:30 IST, is shown in **Error! Reference source not found.**.

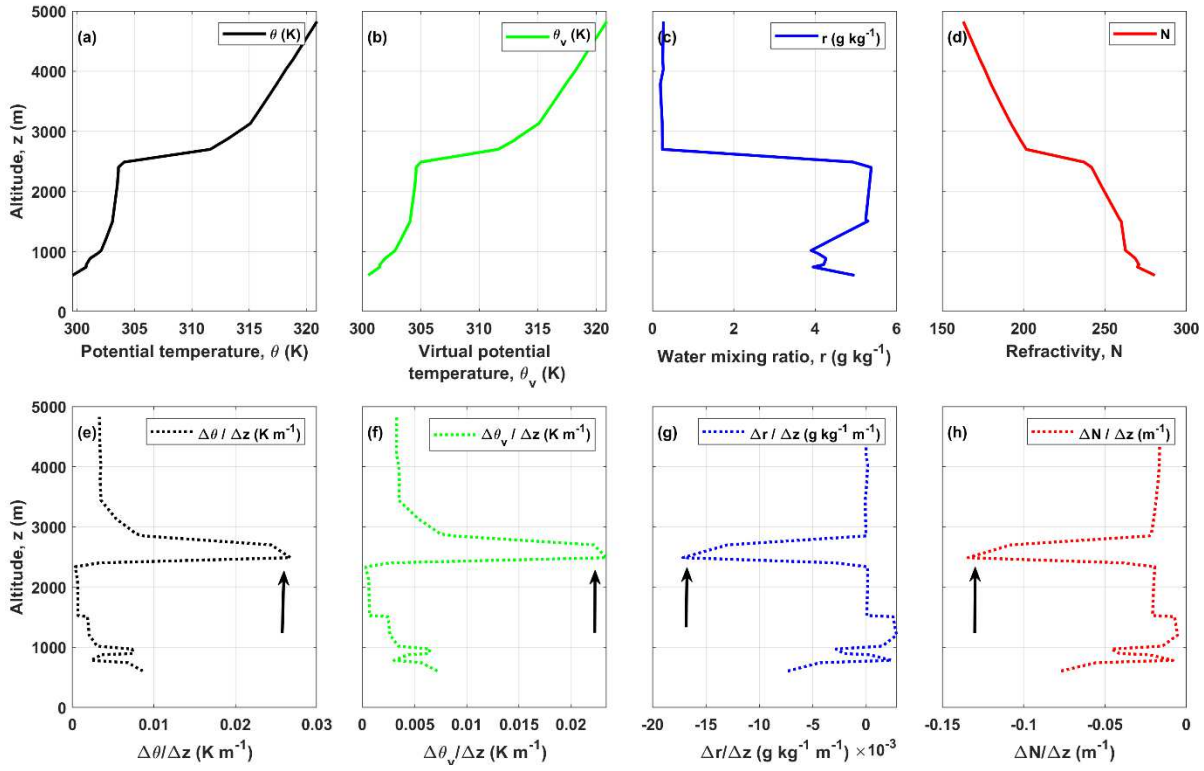


Fig. 4 *Vertical profiles from the Wyoming radiosonde measurement at Nagpur on 17 January 2018, 17:30 IST. The first row of panels shows (a) potential temperature (θ), (b) virtual potential temperature (θ_v), (c) water vapor mixing ratio (r), and (d) refractivity (N). The second row of panels (e–h) presents the corresponding vertical gradients of these variables*

Error! Reference source not found. presents the vertical profiles of potential temperature (θ), virtual potential temperature (θ_v), and water vapor mixing ratio (r) obtained from the radiosonde profile at Nagpur. A notable increase in θ and θ_v, along with a decrease in r, is observed at the altitude of ~2500 m. **Error! Reference source not found.** (e–h) show the gradient of these variables, where the maximum gradient in θ and θ_v (Fig. 4e and f), along with the minimum gradient in r and N (Fig. 5 g and h), marks an Z_i of 2489 m (indicated with a black arrow in **Error! Reference source not found.**e–h). This methodology is applied to all available GPS radiosonde profiles from the nine stations, with Z_i estimated and compared against IMDAA Z_i (Fig. 4). Through the statistical analysis,

it is found that overall, all nine stations, IMDAA shows good agreement with Wyoming radiosonde-derived Z_i. Furthermore, the IMDAA Z_i is in excellent agreement with radiosonde Z_i over Jodhpur, Jagdalpur, Nagpur, and Hyderabad, with R-value (R^2) greater than 0.75 (0.56). In the rest of the stations, the R-value is found to be in the range of 0.52 to 0.68 (Fig. 4a to e). This indicates that IMDAA performs reliably over a broad range of conditions across the Indian region.

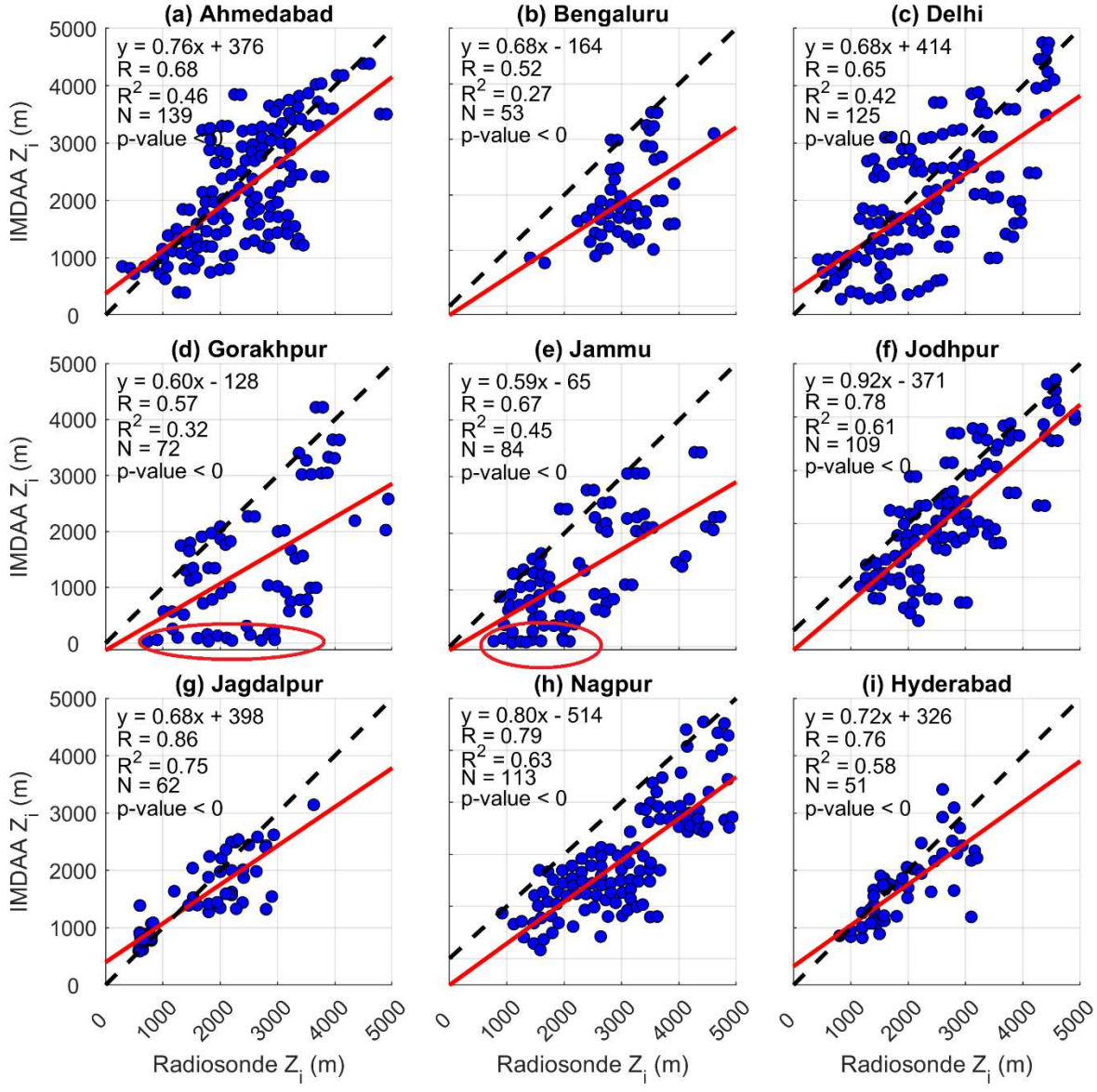


Fig. 4 *Scatter plots between IMDAA Z_i and Wyoming radiosonde Z_i over nine stations across India at 17:30 IST (panels a–i). The red solid line indicates the least-squares linear regression fits, the dashed black line indicates the 1:1 fit, and the red ellipse (in panels d and e) represents the anomalous low IMDAA Z_i values. Here, R is the correlation coefficient, R^2 is the coefficient of determination, and N is the number of data points used for linear regression*

However, at stations Jammu and Gorakhpur, anomalous low (< 100 m; Marked with red ellipse in Fig. 4d and e) IMDAA Z_i with respect to Radiosonde Z_i are observed, which correspond to the December month. It should be noted that these observations correspond to 17:30 IST, a time when the transition of the convective to stable boundary layer occurs. Therefore, the discrepancy may be related to how the stable boundary layer dynamics are represented in IMDAA. In general, the evolution of the stable boundary layer, along with the associated exchanges of mass, momentum, and energy, remains poorly understood and is closely linked to radiation balance (Beljaars, 1998; Tastula et al., 2012; Sterk et al., 2013; Bosveld et al., 2014; Steeneveld, 2014). Furthermore, the boundary layer is also influenced by the radiative cooling at evening time and modulated by the surface net radiation flux. As a result, we suspect that net radiation plays a significant role in influencing the stable boundary layer and may contribute to the discrepancies observed between IMDAA and radiosonde measurements.

To better understand these discrepancies, a comparative assessment was conducted using a reference station, which demonstrated strong agreement between IMDAA and radiosonde Z_i during the same period. Jodhpur is selected as the reference station for this purpose, as it exhibited the highest correlation coefficient (R=0.78, refer to Fig. 4f), a slope close to unity (0.92), and a relatively low intercept bias (371 m), indicating robust performance of IMDAA. The boundary layer dynamics at Jodhpur are then compared against those at Gorakhpur and Jammu during December 2018, where notable underestimation was observed.

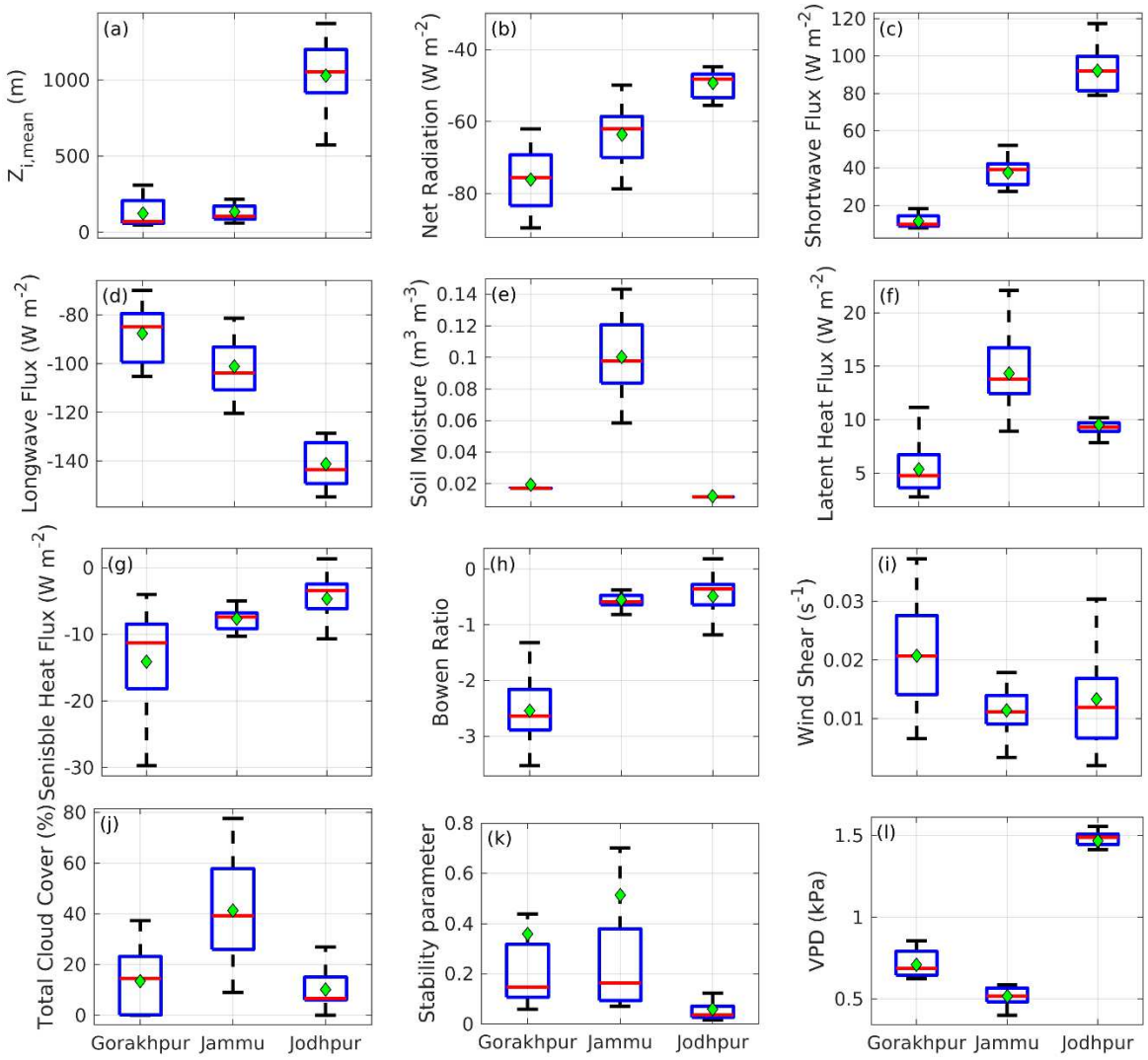


Fig. 5 *Boxplot comparison of Z_i (panel a) and associated surface and atmospheric parameters (panels b to l) at Gorakhpur, Jammu, and Jodhpur locations obtained from IMDAA reanalysis data at 17:30 IST of December 2018. Each box represents the interquartile range (IQR) with the red line indicating the median, whiskers extending to 1.5 times the IQR, and the green diamond represents the mean value for each parameter*

The mean Z_i values were 122 m at Gorakhpur, 134 m at Jammu, and 1028 m at Jodhpur, indicating Jodhpur's boundary layer was approximately eight times deeper (Fig. 5a) than the rest of the two stations. Net radiation, a key component of the surface energy balance, was negative at all three stations, indicating radiative cooling (Fig. 5b). Jodhpur exhibited a less negative net radiation flux (-49.23 W m^{-2}) compared to Gorakhpur (-76.12 W m^{-2}) and Jammu (-63.53 W m^{-2}), implying weaker surface cooling at Jodhpur, which sustains a deeper boundary layer by maintaining convective processes longer into the evening. Stronger cooling at Gorakhpur and Jammu boosts stable stratification, suppressing turbulence and resulting in a shallower boundary layer, supporting the role of net radiation in Z_i discrepancies. Shortwave radiation at Jodhpur (92.5 W m^{-2}) was significantly higher than at Gorakhpur (11.44 W m^{-2}) and Jammu (37.55 W m^{-2}), indicating the incoming shortwave radiation can reach the surface without any interruption over Jodhpur, relatively to Gorakhpur and Jammu (Fig. 5c). It is due to the lower cloud cover at Jodhpur (10.16 %) compared to Gorakhpur (13.5 %) and Jammu (41.31 %). Higher cloud cover at

Gorakhpur and Jammu scatters incoming shortwave radiation, reducing surface heating and convection, contributing to a shallower boundary layer (Fig. 5j). If IMDAA overestimates cloud cover at these sites, it could exaggerate shortwave scattering, further reducing surface energy input and amplifying Z_i underestimation. Net longwave radiation was more negative at Jodhpur (-141.3 W m^{-2}) than at Gorakhpur (-87.57 W m^{-2}) and Jammu (-101.1 W m^{-2}) (Fig. 5d). This again can be attributed to the low cloud cover over Jodhpur, which allows more outgoing longwave radiation to escape, enhancing surface cooling, while higher cloud cover at Gorakhpur and Jammu increases downward longwave radiation, reducing net longwave loss and moderating surface cooling. Overestimated cloud cover could lead to excessive downward longwave radiation, further skewing the energy balance, though the dominant effect remains reduced shortwave heating.

Sensible heat flux was negative at all stations, indicating heat transfer from the atmosphere to a cooler surface (Fig. 5g), promoting stable stratification and suppressing buoyancy-driven turbulence, resulting in a shallow boundary layer, particularly at Gorakhpur and Jammu. Latent heat flux varied (Fig. 5f), with Jammu showing the highest (14.32 W m^{-2}), corresponding to higher soil moisture of 0.1 m^3 m^{-3} (Fig. 5e), supporting greater evaporation. Jodhpur, despite having lower soil moisture of 0.012 m^3 m^{-3} and comparable to Gorakhpur (0.019 m^3 m^{-3}), the latent heat flux is 9.5 W m^{-2}, which is almost two-fold higher than Gorakhpur's latent heat flux of 5.3 W m^{-2} (Fig. 5f). This is attributed to the relatively dry conditions over Jodhpur, where the vapor pressure deficit (VPD) is higher at 1.46 kPa, compared to the more humid environment in Gorakhpur with a vapor pressure deficit of 0.70 kPa (Fig. 5l). A higher VPD enhances the evaporative gradient, promoting stronger latent heat flux even with limited soil moisture, indicating that atmospheric demand significantly influences latent heat flux. Overestimated cloud cover could indirectly reduce VPD by limiting surface heating, further suppressing latent heat flux at Gorakhpur and contributing to a shallower boundary layer. The negative Bowen ratio at all stations, due to negative sensible heat flux, confirms stable stratification, as warm air over a cooler surface inhibits vertical mixing, maintaining a shallow boundary layer. Wind shear, a proxy for mechanical turbulence, was similar at Jammu (0.011 s^{-1}) and Jodhpur (0.013 s^{-1}) but slightly higher at Gorakhpur (0.02 s^{-1}) (Fig. 5i). However, the stability parameter (zL^{-1}) at Gorakhpur (mean=0.35, median=0.15) and Jammu (mean=0.51, median=0.16) was 6 to 8 folds higher than at Jodhpur (mean=0.06, median=0.03), indicating stronger stability at Gorakhpur and Jammu (Fig. 5k), which, in addition to the natural diurnal cycle, is further enhanced by reduced surface heating and higher cloud cover, leading to stronger boundary layer decay.

These evidences suggest that the IMDAA simulates boundary layer dynamics in semi-arid, clear-sky conditions like Jodhpur fairly well, where low cloud cover and high shortwave radiation sustain a deeper boundary layer. However, in cloudier, humid subtropical climatic regions like Gorakhpur and Jammu, IMDAA underestimates Z_i, likely due to multiple factors, including potential overestimation of cloud cover, which reduces incoming surface-reaching shortwave radiation, increases stability, and skews the surface energy balance. Additionally, during the late-afternoon transition to a stable boundary layer, IMDAA may overestimate stability or struggle to resolve weak turbulence, leading to premature boundary layer collapse, potentially exacerbated by excessive cloud cover effects. In addition, the surface roughness length in IMDAA is assumed to be a constant value of 0.5 (plot not shown). Since energy balance closure depends on surface roughness length, this assumption could have also contributed to the observed discrepancy between Z_i from IMDAA and that from radiosonde observations (Anand et al., 2022). These results suggest that differences in net radiation and cloud cover, particularly over the humid

subtropical region, may influence the reliability of IMDAA Z_i estimates across different meteorological and geographical conditions. Apart from these challenges, the IMDAA demonstrates robust performance in accurately capturing the Z_i over the rest of the Indian region, as shown through the cross-validation of Z_i derived from IMDAA against radiosonde observations from multiple Indian sites. Hence, IMDAA Z_i is utilized to investigate the seasonal, diurnal, and spatial variability of the daily $Z_{i,max}$ over the Indian region in the next section.

3.2 Variability of $Z_{i,max}$ over the Indian Region

$Z_{i,max}$ is the daily maximum value of the boundary layer height and represents the most convectively developed state of the boundary layer for that day, and can serve as an effective indicator for the peak vertical mixing and convective activity. Furthermore, as a proxy for surface heating, the $Z_{i,max}$ reflects the strength of thermally driven turbulence within the boundary layer and vital for air quality studies, as a higher (lower) $Z_{i,max}$ amplifies (lowers) the vertical dispersion of pollutants, reducing (increasing) their concentration near the surface; provided if the terrain is flat and in absence of temperature inversion.

Hence, characterizing $Z_{i,max}$ is essential for understanding the extent of vertical mixing in the atmosphere, which directly influences surface-atmosphere exchange processes. For this purpose, we used IMDAA reanalysis data to estimate the $Z_{i,max}$. For each grid point (12 km × 12 km), and for each day, the maximum value of Z_i was extracted, representing the most convectively developed state of the boundary layer for that day. Subsequently, we calculated the seasonal mean of $Z_{i,max}$ values to study its spatial variability of boundary layer development across different seasons. Along with $Z_{i,max}$, it's time of occurrence in each region (i.e., the time of the day during which Z_i reaches maximum value in the region) is vital. The spatial and seasonal variations of the $Z_{i,max}$, thus obtained, are shown in Fig. 7 for the Indian region.

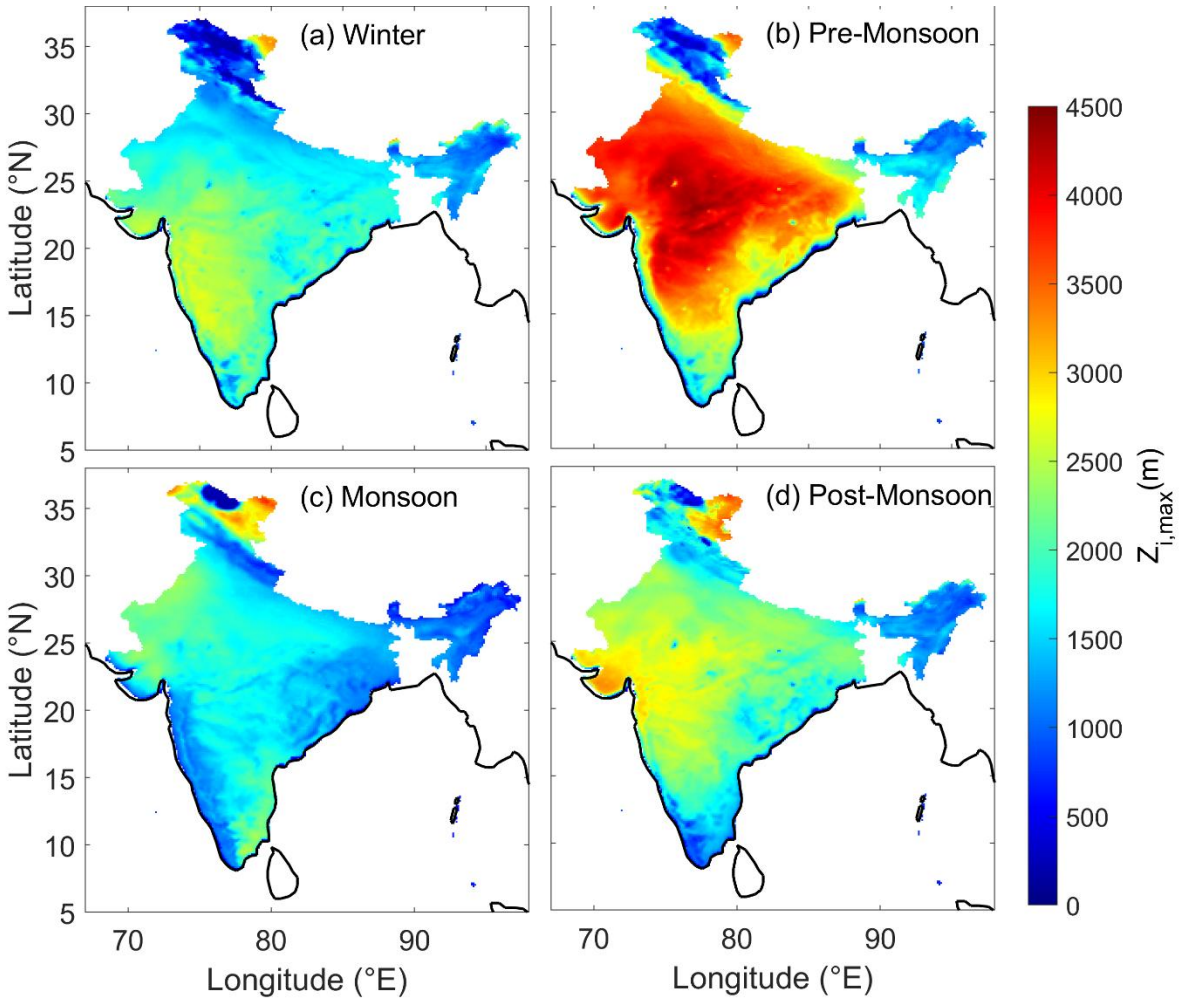


Fig. 6 *Seasonal $Z_{i,max}$ over the Indian region from IMDAA during 2018*

The Fig.s reveal pronounced spatial and seasonal variability of daily $Z_{i,max}$ over the Indian region (Fig. 6). In the winter season (DJF), $Z_{i,max}$ remains relatively low across the subcontinent, with the shallowest boundary layer found over Kashmir, and where values are often below 500 m (Fig. 6a). This shallow boundary layer extends eastward into northeast India, where the value ranges between 500 and 1000 m. Central and southern India shows a relatively deeper boundary layer, with $Z_{i,max}$ generally ranging from 2000 to 2500 m, and reaching up to 2700 m around the Western Ghats, possibly due to orography lifting. As the pre-monsoon season (MAM) arrives, there is a substantial increase in $Z_{i,max}$ across the country (Fig. 6b). This season records the highest $Z_{i,max}$ values of the year, with extensive regions over northwest, central, and parts of northern India exhibiting values above 4000 m and even exceeding 4500 m in certain areas. The southern peninsula shows relatively lower $Z_{i,max,}$ in the range between 1500 and 2500 m. During the monsoon season (JJAS), $Z_{i,max}$ undergoes a marked reduction across the sub-continent, with values generally between 1000–2000 m across much of the country, except northeast of the Kashmir region, where the $Z_{i,max}$ of up to 3500 m is observed (Fig. 6c). The northeastern states, parts of eastern India, and the Himalayan foothills show notably suppressed $Z_{i,max}$ (<1000 m), while western and southern India maintain moderately higher values of around 2000 m. In the post-monsoon season (OND), the $Z_{i,max}$ begins to increase slightly from the monsoon minimum but remains modest, with central and western India showing values around 2500–3000 m (Fig. 6d). Overall, the pre-monsoon season stands out for its deep boundary layers, while

winter and post-monsoon seasons are characterized by widespread shallow ABL. Spatially, western and central India consistently experience higher boundary layer development, while northern and northeastern regions remain comparatively suppressed across most seasons.

In general, the growth of the boundary layer is highly modulated by factors like soil moisture, surface albedo, sensible and latent heat flux, surface temperature, etc. (Pleim and Xiu, 1995; Kim and Entekhabi, 1998; Basara and Crawford, 2002). Hence, to further understand the observed variations in $Z_{i,max}$, corresponding seasonal mean sensible heat net flux (Fig. S1), latent heat net flux (Fig. S2), Bowen ratio (Fig. S3), soil moisture (Fig. S4), and total precipitation (Fig. S5), wind speed (Fig. S6) from IMDAA is considered. The low boundary layer height ($Z_{i,max}$ < 500 m) observed in Kashmir during winter is driven by minimal or negative sensible heat flux (often < 0 W m^{-2}), where heat transfers from the atmosphere to the colder surface, such as snow-covered ground. This process suppresses convection-driven turbulence, stabilizing the boundary layer and limiting its vertical growth. High-pressure systems prevalent in the region, as evident from diverging wind (Fig. S6), further enhance stability by causing subsidence, sinking air that compresses the boundary layer and inhibits mixing. A similar pattern occurs in northeast India, where $Z_{i,max}$ ranges between 500–1000 m. Here, negative sensible heat flux and high-pressure systems dominate, reducing convective activity and maintaining a relatively shallow boundary layer due to limited surface heating.

In contrast, the Western Ghats exhibit a peak boundary layer height ($Z_{i,max}$ up to 2700 m) (Fig. 6a), driven by a high Bowen ratio (> 10) (Fig. S3a). The Bowen ratio, which compares sensible heat flux (direct heating of the air) to latent heat flux (energy used for evaporation), indicates that most available energy in the Western Ghats is used for sensible heating. This strong heating warms the near-surface air, intensifying turbulence and convection, which deepens the boundary layer. Conversely, in Tamil Nadu (eastern peninsular India), a high sensible heat flux (90 W m^{-2}) is observed, but a lower Bowen ratio (2–6) shows that a significant portion of energy is diverted to latent heat flux for evaporation, particularly due to moist coastal conditions. This reduces the energy available for convection, resulting in weaker turbulence and relatively low $Z_{i,max}$ compared to the Western Ghats. The central and southern India deeper boundary layer, typically $Z_{i,max}$ ranging between 2000–2500 m, and over the Western Ghats, it peaked to 2700 m.

Among the four seasons, the $Z_{i,max}$ of ~4500 m is observed over the central Indian region during pre-monsoon (Fig. 6b) and consistent with the previous study based on the MERRA-2 dataset, where Z_i up to ~4000 m was reported (Sathyanadh et al., 2017). It is attributed to a very low soil moisture of less than 0.05 m^3 m^{-3} (Fig. S4b). Subsequently, it led to a high sensible heat flux greater than 100 Wm^{-2} (Fig. S1b), a low latent heat flux of less than 40 Wm^{-2} (Fig. S2b), and a Bowen ratio greater than 2, suggesting most of the available surface energy is manifested more into sensible heat flux and contributing to the convective turbulent mixing (Fig. S3b). In contrast, Brahmanandam et al. (2020) reported the seasonal mean $Z_{i,max}$ (up to 3000 m) in northern India instead of central India using COSMIC-RO observations. This discrepancy may arise because COSMIC-RO profiles degrade near the surface due to water vapor interference in the lower atmosphere, making them less reliable for detecting the shallow boundary layer. Consequently, excluding these potentially low Z_i profiles can bias the dataset toward deeper boundary layers, resulting in an overestimation of seasonal mean $Z_{i,max}$ in northern India. During the same season, a high net flux of sensible heat (>120 W m^{-2}) is observed along the coastal region of peninsular India, exceeding values recorded over parts of central India, where the $Z_{i,max}$ up to 4500 m, is observed (Fig. S1b).

Despite the relatively high sensible heat flux along the coast, the $Z_{i,max}$ remains below 2000 m in this region (Fig. 6b), suggesting that factors other than surface heating influence boundary layer development. This is consistent with earlier studies that report Bowen ratios below unity over most of India, particularly in coastal regions, due to higher latent fluxes and proximity to the ocean (e.g., Puygrenier et al., 2005; Anurose et al., 2018). The suppressed $Z_{i,max}$ along the coast may also be attributed to sea-breeze-induced formation of internal boundary layers and low to mid-level clouds, which inhibit vertical mixing between the surface and the free atmosphere. These results are broadly consistent with previous observations and support existing understanding of coastal boundary layer dynamics (Kunhikrishnan et al., 1993; Moorthy et al., 1993; Babu and Moorthy, 2001; Rani et al., 2010).

Another interesting observation is that in the central Indian region, there is no notable difference in latent heat flux between winter and pre-monsoon seasons due to consistent soil moisture (Fig. S4a and b). However, during the transition from winter to pre-monsoon, sensible heat flux increases significantly from ~80 W m^{-2} to ~120 W m^{-2}, driven by longer daylight hours and greater solar insolation (Fig. S7). This rise in sensible heat flux increases surface heating, promoting turbulence and convection in the boundary layer. A strong coefficient of determination ($R^2 = 0.65$) between sensible heat flux and daily solar insolation supports this relationship (Fig. S7a).Furthermore, the Bowen ratio, which indicates surface energy partitioning between sensible and latent heat fluxes, exceeds 10 over western India (Fig. 6b), signifying that most surface energy contributes to sensible heat flux, warming the near-surface air. Surprisingly, the peak $Z_{i,max}$ occurs over central India instead of over western India, suggesting that the magnitude of sensible heat flux, rather than the Bowen ratio alone, primarily drives $Z_{i,max}$ variability. To investigate this, linear regression was performed between sensible heat flux and $Z_{i,max}$, and between Bowen ratio and $Z_{i,max}$, for central India (24°N, 77°E) and western India (24°N, 77°E). In central India, a strong correlation ($R^2 = 0.69$, 95% confidence level) exists between sensible heat flux and $Z_{i,max}$, indicating that higher sensible heat flux strengthens turbulence and convection, deepening the boundary layer (Fig. 7a). However, the correlation between Bowen ratio and $Z_{i,max}$ is weak ($R^2 = 0.16$), suggesting limited influence (Fig. 7b). In western India, sensible heat flux also correlates well with $Z_{i,max}$ ($R^2 = 0.66$) (Fig. 7c), while the Bowen ratio shows a moderate correlation ($R^2 = 0.51$) (Fig. 7d), performing better than in central India but still less influential than sensible heat flux. These results highlight that sensible heat flux, by directly fuelling convective mixing, is the dominant driver of $Z_{i,max}$ variability than the Bowen ratio in central India.

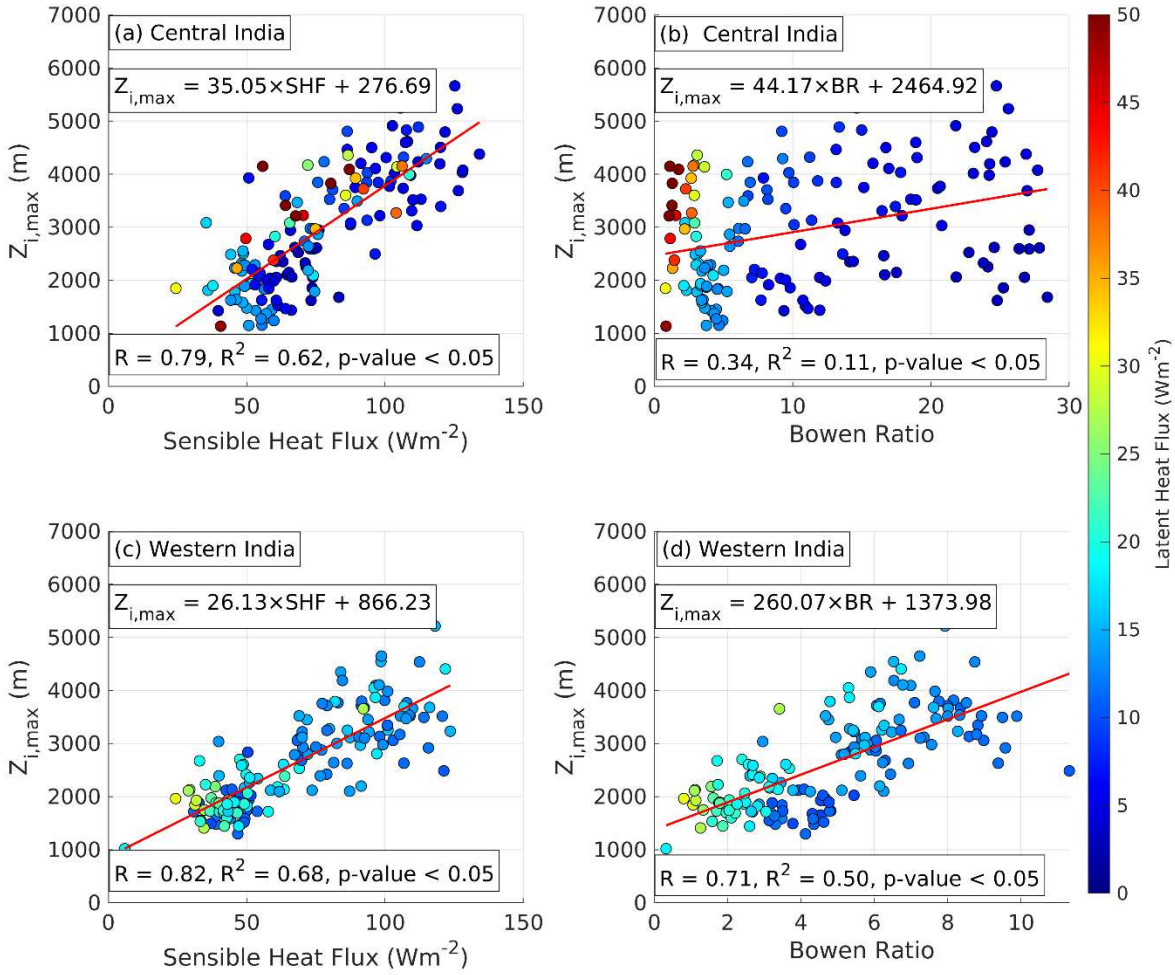


***Fig.** 7 Scatter plots showing the relationship between $Z_{i,max}$, and (a, c) sensible heat flux, and (b, d) Bowen ratio for (a, b) central India (24°N, 77°E) and (c, d) western India (24°N, 77°E). The red lines represent linear regression fits, with correlation coefficient (R) and coefficient of determination (R^2) indicating the strength of the relationship. P-value < 0.05 denotes statistical significance at the 95 % confidence level. The color of each data point represents latent heat flux (W m^{-2})*

During monsoon season, due to an increase in precipitation (except in northwest and southeast Indian regions), the soil moisture has increased by greater than 0.4 m^3 m^{-3} (Fig. S4c and Fig. S5c). It resulted in increased latent heat flux and decreased sensible heat flux with a Bowen ratio of less than 0.8 over most of these regions (Fig. S3c). These changes manifested into a shallow boundary layer with a $Z_{i,max}$ less than 1500 m (Fig. 6c). The highest $Z_{i,max}$ of up to ~2500 m is observed in the northwest Indian region (Fig. 6c) owing to low soil moisture of less than 0.05 m^3 m^{-3} (Fig. S4c) and subsequent, high sensible heat flux of ~90 Wm^{-2} (Fig. S1c) and low latent heat flux of ~50 Wm^{-2} (Fig. S2c). But during the post-monsoon, the $Z_{i,max}$ became relatively shallower over the southern peninsular region and deeper over the central Indian regions (Fig. 6c and d). Overall, we report that the magnitude of $Z_{i,max}$ depends more on sensible heat flux over inland regions than coastal regions, where sea-breeze interactions may suppress ABL growth despite the high availability of sensible heat flux. In addition, in the peninsular Indian

region, a strong zonal variation of the $Z_{i,max}$ is observed, such that $Z_{i,max}$ increases from west to inland and afterward decreases towards the east.

To explore the zonal variations further, five diverse locations which capture the strong zonal variation of $Z_{i,max}$ along the latitude of ~12.9°N are chosen, as this latitude spans varied geographic features, making it suitable for study zonal variations: two coastal locations Mangaluru (12.9°N, 74.8°E) and Chennai (13.08°N, 80.27°E), two oceanic locations Arabian Sea (12.9°N, 72°E) and Bay of Bengal (12.9°N, 82°E), and one inland location Bengaluru (12.97°N, 77.58°E), and corresponding mean diurnal variations for all seasons is shown inFig. 8.

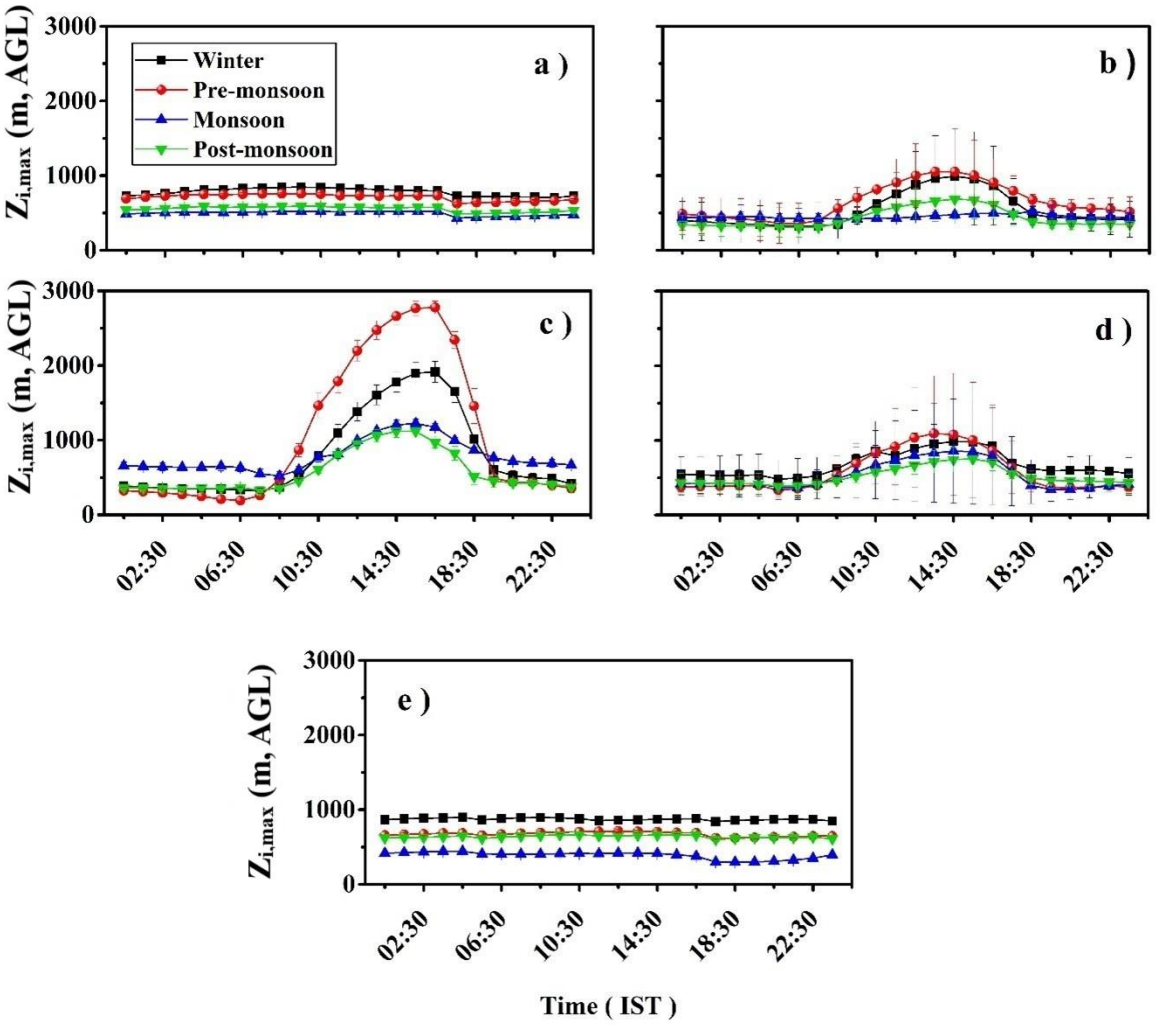


Fig. 8 *Seasonality in the diurnal variations of IMDAA $Z_{i,max}$ for the region (a) Arabian Sea (12.9°N, 72°E), (b) Mangaluru (12.9°N, 74.8°E), (c) Bengaluru (12.97°N, 77.58°E), (d) Chennai (13.08°N, 80.27°E), and (e) Bay of Bengal (12.9°N, 82°E). (AGL = Above Ground Level). The error bars represent the standard deviation of $Z_{i,max}$*

Among these locations, Bengaluru exhibited strongest diurnal variation during all seasons, such that $Z_{i,max}$ peaked up to 3000 m by 16:30 (IST) during pre-monsoon, associated with the low specific heat capacity of the land surface (Fig. 8c); whereas over the Arabian Sea and Bay of Bengal the diurnal variations were extremely weak, if not nil, during all the four seasons; attributed to the marine environment with high specific heat capacity and vertical turbulent mixing of oceanic water (Fig. 8a and e). Though Mangalore and Chennai showed moderate

diurnal variation, a large standard deviation in the hourly $Z_{i,max}$ is observed (Fig. 8b and d). It could be possibly due to pulsated sea breeze, which oscillates at an hourly frequency affecting atmospheric stability, and thus $Z_{i,max}$ (Puygrenier et al., 2005; Anurose et al., 2018). However, further investigation is needed to confirm this mechanism. In contrast, the hourly standard deviation of $Z_{i,max}$ over Bengaluru, is extremely minimal (Fig. 8c). This indicates that over this region, the surface and atmospheric conditions remain relatively consistent across days within each season. This could possibly be due to stable synoptic patterns or uniform land-atmosphere interactions over Bengaluru during those periods. Furthermore, in both coastal regions (Chennai and Mangaluru), the $Z_{i,max}$ occurs at 13:30 IST (Fig. 8b and d), which is three hours earlier than in the Bengaluru region, indicating a strong spatial variation in the timing of $Z_{i,max}$. This indicates that the time of occurrence of the $Z_{i,max}$ is not the same over various regions. Precise knowledge of the time of occurrence of $Z_{i,max}$ is an absolute necessity for managing air quality, predicting extreme weather, and refining climate models. Hence, the variability of the time of occurrence of the $Z_{i,max}$ over the Indian region is analyzed, and the results are discussed in the next section.

3.3 Seasonal variability in the time of occurrence of the $Z_{i,max}$

The time of occurrence of the $Z_{i,max}$ indicates the peak of convective mixing, which controls pollutant dispersion, heat and moisture transport, and the initiation of weather systems, directly impacting human health, agriculture, and disaster preparedness. Given its importance, a spatial variation of the time of occurrence of $Z_{i,max}$ for the whole Indian region, is studied for all the seasons (Fig. 9). Fig. 9 readily conveys that the time of occurrence of the $Z_{i,max}$ undergoes seasonal variation along with spatial variation. The $Z_{i,max}$ is attained as early as 12:30 IST in the northeast Indian region for all seasons (Fig. 9) and as late as 17:30 IST in the Western Ghats during monsoon (Fig. 9c). Despite the extremity in time of occurrence of $Z_{i,max}$, the Bowen ratio of these two regions is less than 1 and comparable in magnitude during this season (Fig. S3c). Furthermore, both regions share the same magnitude of soil moisture, sensible and latent heat fluxes, and even magnitude of $Z_{i,max}$ being less than 1000 m (Fig. 6c). It suggests that even though surface energy partition and $Z_{i,max}$ attained at these regions are the same, the growth rate of the boundary layer over the Western Ghats is slower than northeast Indian region. This could be due to the southwest monsoon circulation, which brings moist air masses from the Arabian Sea to the western ghats (Fig. S6c), forming low altitude clouds (Fig. S8c) and thus suppressing the growth of the boundary layer (Fig. 6c) (Srinivas et al., 2015). In the rest of the three seasons, the Z_i reached its maximum value relatively earlier (i.e., between 14:30 IST to 15:30 IST) over the western ghats (Fig. 9), but no notable change has been observed over the northeast Indian region, highlighting significance of the monsoon circulation in defining the growth rate of boundary layer and thus the time of occurrence of $Z_{i,max}$ over the western ghats. During the winter season, along the northwest, central, and peninsular India, the $Z_{i,max}$ occurs at ~16:30 IST, and in the northeast Indian region, it occurs early at ~14:30 IST (Fig. 9a). During post-monsoon, over most of the Indian region, the $Z_{i,max}$ is attained by ~15:30 IST (Fig. 9d).

It is evident that 15:30 IST is the most common time for the occurrence of $Z_{i,max}$ across most of India during winter and post-monsoon season (Fig. 10a and d). During the pre-monsoon and monsoon seasons, the frequency of $Z_{i,max}$ occurring at 15:30 IST and 16:30 IST, is comparable (Fig. 10b and c). However, when considering all seasons collectively, the most common time for the occurrence of $Z_{i,max}$ (i.e., fully developed boundary layer) is around

15:30 IST across the entire Indian region, suggesting that the radiosonde launch time of 14:00 IST in the earlier study (Kannemadugu, 2024) may have preceded the peak boundary layer development in some regions.

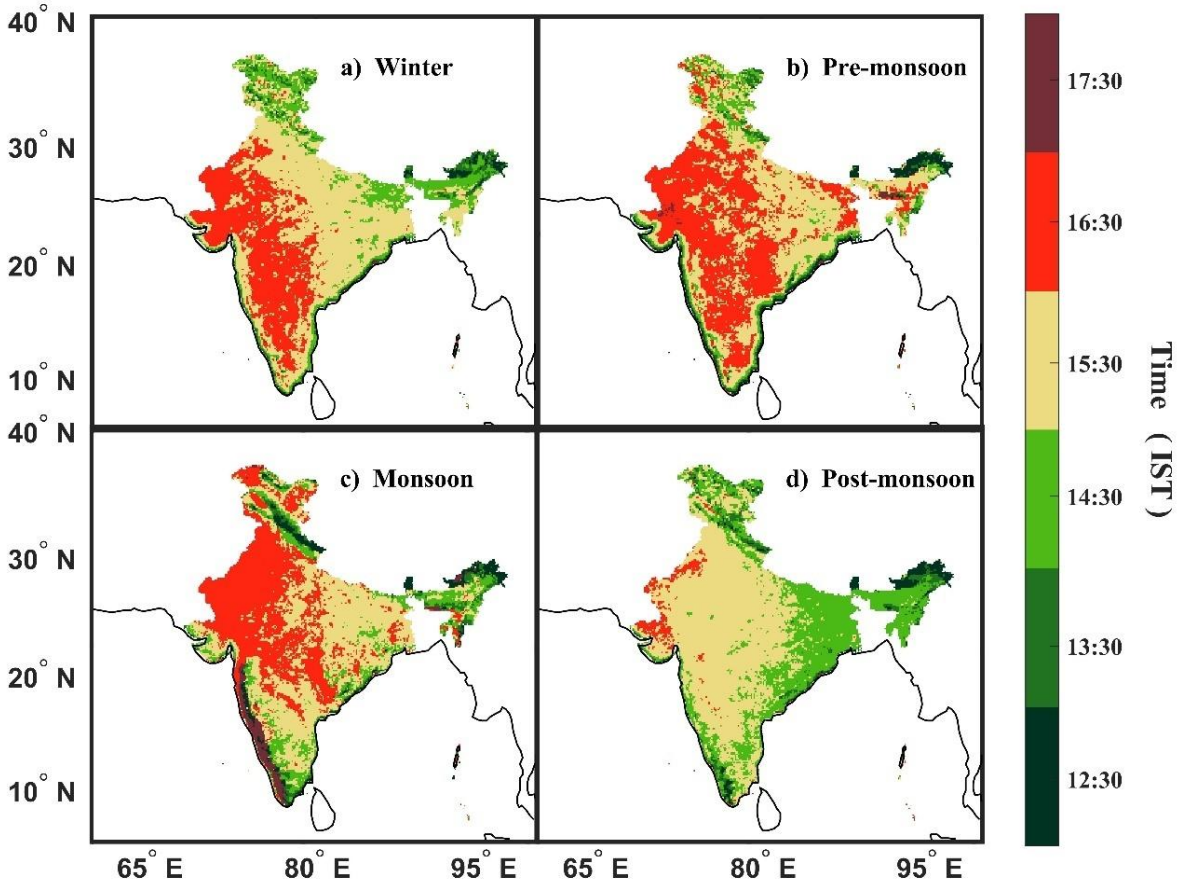


Fig. 9 *Time of occurrence of the $Z_{i,max}$ obtained from IMDAA over India for (a) Winter, (b) Pre-monsoon, (c) Monsoon, and (d) Post-monsoon seasons are shown. The vertical bar represents the time (IST)*

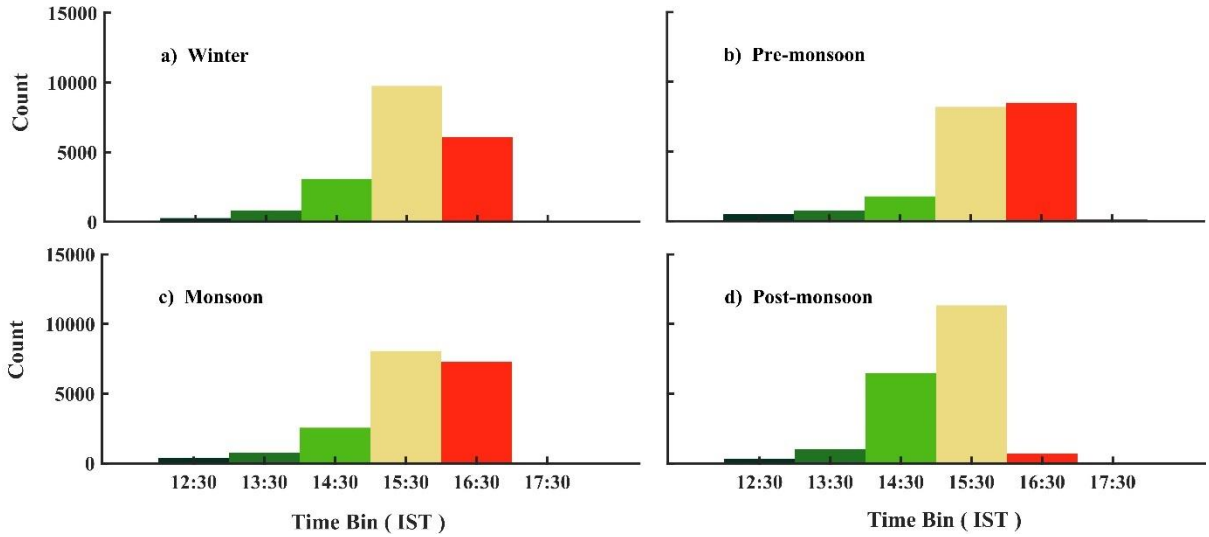


Fig. 10 *Histogram of time of occurrence of IMDAA $Z_{i,max}$ over India for (a) Winter, (b) Pre-monsoon, (c) Monsoon, and (d) Post-monsoon seasons is shown*

Based on this, we considered 15:30 IST as the standard time for the occurrence of $Z_{i,max}$ over the Indian region. Subsequently, we define a three-hour time interval as 00:30, 03:30, 06:30, 09:30, 12:30, 15:30, 18:30, and 21:30 IST for further analysis. Fig. 11 represents the spatial pattern of diurnal variation of Z_i from 00:30 to 09:30 IST over the Indian subcontinent for all seasons. Owing to the radiative cooling of the surface and atmospheric stability, the shallow Z_i (<~500 m) occurred between 00:30 and 06:30 IST over India during all four seasons (Fig. 11). After sunrise, due to the availability of solar radiation, corresponding surface heating, and increased convection, the Z_i starts increasing gradually around 9:30 IST, and it peaked up to ~2500 m over central India during the pre-monsoon season (Fig. 11). However, there is no significant increase in Z_i detected until 9:30 IST during the post-monsoon and winter season. At 12:30 IST, due to an increase in intense solar activity, the Z_i of central India in pre-monsoon reaches ~ 3500 m (Fig. 11).

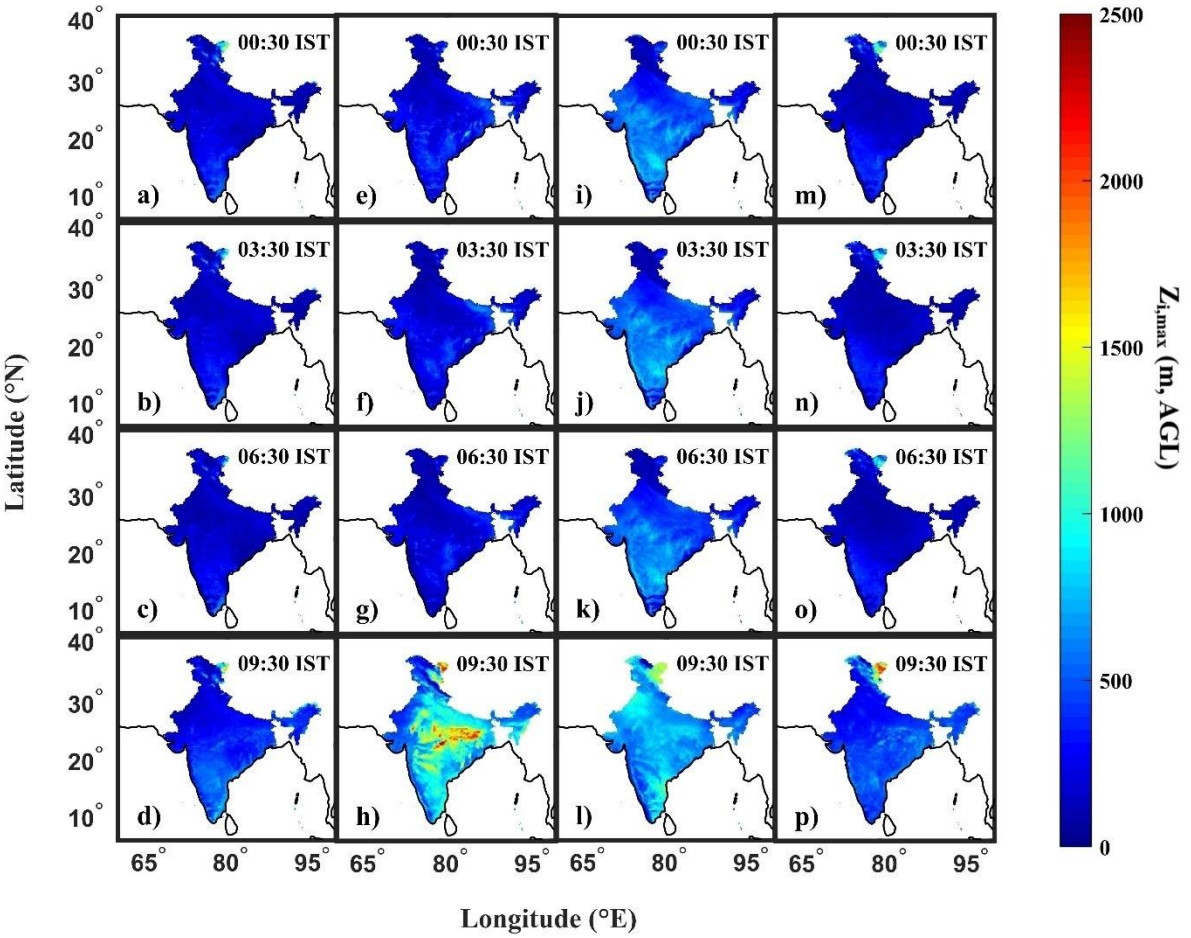


Fig. 11 *Spatial pattern of seasonality in the hourly average of $Z_{i,max}$ from 0:30 to 9:30 IST was obtained from IMDAA in 2018. The first, second, third, and fourth columns correspond to the winter, pre-monsoon, monsoon, and post-monsoon seasons, respectively. Here, 'AGL' stands for Above Ground Level*

At 15:30 IST, the Z_i over the northwest desert region reaches a peak value of ~2500 m during the monsoon and post-monsoon seasons, and over the central Indian region, it reaches a peak greater than 2500 m during the winter and pre-monsoon seasons (Fig. 13). The observed highest (~ 4500 m) and lowest (~ 80 m) Z_i during the pre-monsoon season indicate greater variability in Z_i compared to other seasons. After reaching its maximum around 15:30 IST, the Z_i gradually decreases until 18:30 IST, after which it stabilizes at a shallow height due to the onset of stable atmospheric conditions.

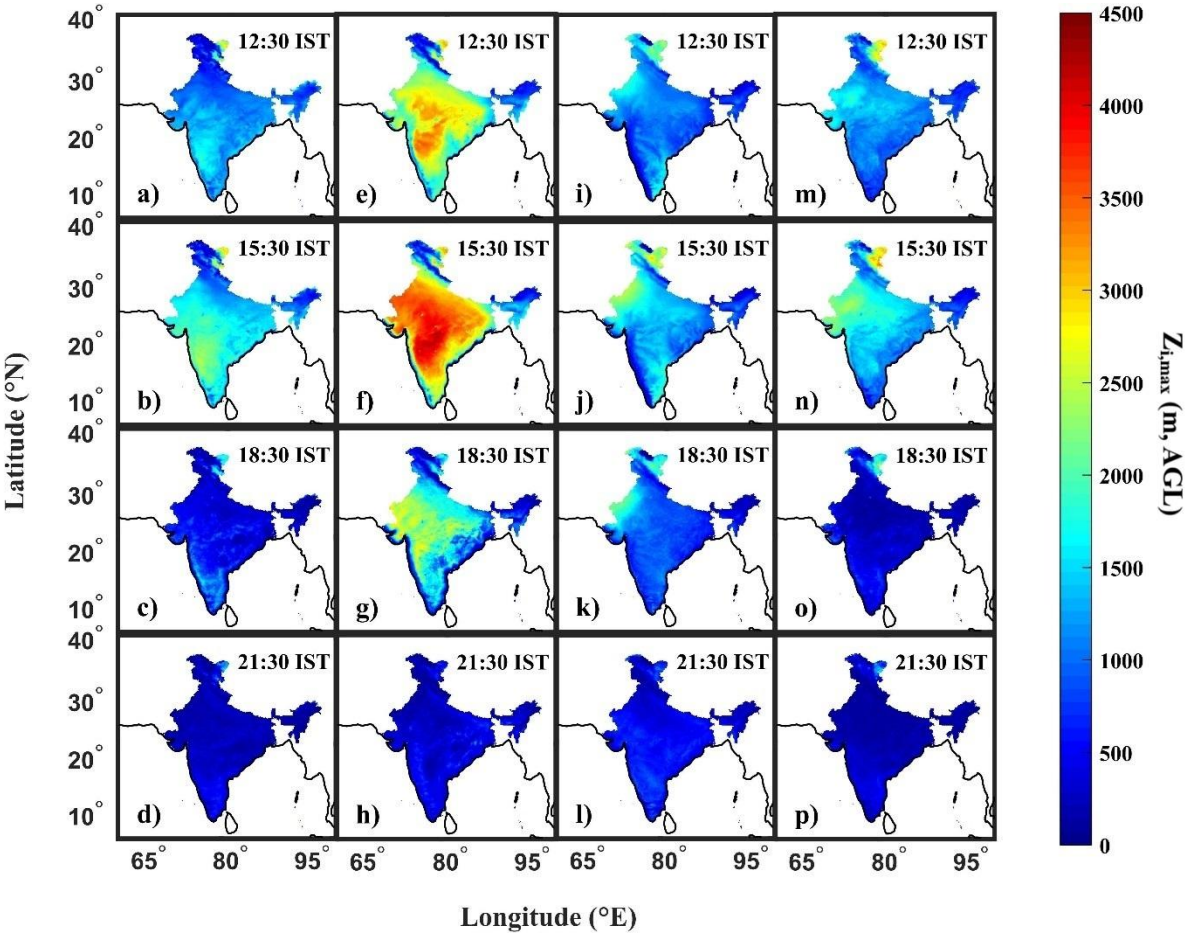


Fig. 12 *Same as Fig. 12 but for the time period from 12:30 IST to 21:30 IST.*

During all seasons, Z_i starts growing from ~07:30 IST, and it gradually attains peak value by 15:30 IST and decreases rapidly until 18:30 IST, which implies the decay is faster than the growth of Z_i. Despite the highest mean Z_i during pre-monsoon, a large fluctuation in the Z_i reflects the existence of highly unstable atmospheric conditions over the Indian region. The diurnal variation during the monsoon season is weakest among all other seasons, with a maximum mean Z_i of ~1500 m.

4. Summary and conclusion

In summary, we have evaluated the performance of the IMDAA's atmospheric boundary layer height (Z_i) using multi-platform observations, and characteristics of the $Z_{i,max}$ over the Indian region are studied. A consolidated key finding of these analyses and observations are listed as follows:

1. The results show that IMDAA outperforms ERA5 and is in good agreement with GPS radiosonde and COSMIC-RO measurements. Further validation of IMDAA Z_i against nine inland Wyoming radiosonde stations revealed that IMDAA Z_i is in good agreement with radiosonde Z_i and captures seasonal variabilities well.

2. Over Jammu and Gorakhpur in December, IMDAA strongly underestimates Zi (<100 m) compared to radiosonde values (1000–2000 m) due to excessively negative net radiation, negative sensible heat flux, enhanced static stability, and likely excessive low-cloud cover; these factors cause premature surface cooling, suppressed turbulence, and early collapse of the convective boundary layer.

3. Daily maximum boundary layer height ($Z_{i,max}$) exhibits pronounced spatial and seasonal variability across India: deepest (>4500 m) during pre-monsoon over central and northwest India, driven by intense sensible heating and dry conditions; shallowest (<500 m) in winter and post-monsoon, particularly over Kashmir and Northeast India; elevated over the Western Ghats due to high Bowen ratios; and comparatively suppressed along moist coasts (e.g., Tamil Nadu) despite strong surface heating, owing to dominant latent heat flux. Over central India, $Z_{i,max}$ is primarily governed by sensible heat flux, whereas over western India, both sensible heat flux and Bowen ratio contribute nearly equally. Overall, $Z_{i,max}$ is tightly regulated by surface energy partitioning, soil moisture, and Bowen ratio, highlighting its vital importance for air quality forecasting, weather prediction, and surface–atmosphere interaction studies over the Indian subcontinent.

4. Diurnal evolution of the boundary layer across India shows that the fully developed convective boundary layer ($Z_{i,max}$) consistently peaks around 15:30 IST in all seasons, indicating that radiosonde launches near this time would best capture the mature daytime boundary layer, maximum vertical mixing, and peak pollutant dispersion more effectively than early-morning or late-evening ascents.

Author contributions

Prasanth and Gayathri have conceived the work and carried out the scientific data analysis and were involved in the scientific interpretation of the results, leading to the formulation of the manuscript. All authors reviewed the manuscript.

Acknowledgement

We acknowledge the mission scientists of IMDAA (for the ABLH), ERA5 (for ABLH), Wyoming (for radiosonde observations), NARL (for radiosonde observations), COSMIC GPS-RO (for the refractivity profiles), as well as the associated personnel, for the data used in this work

Reference

Anand, N., Satheesh, S.K., Moorthy, K.K., 2022. Land-Atmosphere Interactions at a Semi-Arid Region in the Deccan Plateau. Journal of Geophysical Research: Atmospheres 127, e2022JD037211. https://doi.org/10.1029/2022JD037211

Babu, S.S., Moorthy, K.K., 2001. Anthropogenic impact on aerosol black carbon mass concentration at a tropical coastal station: A case study. Curr Sci 1208–1214.

Basara, J.B., Crawford, K.C., 2002. Linear relationships between root-zone soil moisture and atmospheric processes in the planetary boundary layer. Journal of Geophysical Research: Atmospheres 107, ACL 10-1. https://doi.org/10.1029/2001JD000633

Basha, G., Ratnam, M.V., 2009. Identification of atmospheric boundary layer height over a tropical station using high-resolution radiosonde refractivity profiles: Comparison with GPS radio occultation measurements. Journal of Geophysical Research: Atmospheres 114, 16101. https://doi.org/10.1029/2008JD011692

Beyrich, F., 1997. Mixing height estimation from sodar data — A critical discussion. Atmos Environ 31, 3941–3953. https://doi.org/10.1016/S1352-2310(97)00231-8

Bhumralkar, C.M., 1976. Parameterization of the planetary boundary layer in atmospheric general circulation models. Reviews of Geophysics 14, 215–226.

Bianco, L., Wilczak, J.M., 2002. Convective boundary layer depth: Improved measurement by Doppler radar wind profiler using fuzzy logic methods. J Atmos Ocean Technol 19, 1745–1758.

Brahmanandam, P.S., Kumar, V.N., Kumar, G.A., Rao, M.P., Samatha, K., Ram, S.T., 2020. A few important features of global atmospheric boundary layer heights estimated using COSMIC radio occultation retrieved data. Indian Journal of Physics 94, 555–563. https://doi.org/10.1007/S12648-019-01514-7/FIG.S/5

Budakoti, S., Singh, C., 2021. Examining the characteristics of planetary boundary layer height and its relationship with atmospheric parameters over Indian sub-continent. Atmos Res 264, 105854.

Chan, K.M., Wood, R., 2013. The seasonal cycle of planetary boundary layer depth determined using COSMIC radio occultation data. Journal of Geophysical Research: Atmospheres 118, 12,422-12,434. https://doi.org/10.1002/2013JD020147

Dee, D.P., Uppala, S.M., Simmons, A.J., Berrisford, P., Poli, P., Kobayashi, S., Andrae, U., Balmaseda, M.A., Balsamo, G., Bauer, d P., 2011. The ERA-Interim reanalysis: Configuration and performance of the data assimilation system. Quarterly Journal of the royal meteorological society 137, 553–597.

Dias-Júnior, C.Q., Carneiro, R.G., Fisch, G., D'Oliveira, F.A.F., Sörgel, M., Botía, S., Machado, L.A.T., Wolff, S., Santos, R.M.N. dos, Pöhlker, C., 2022. Intercomparison of planetary boundary layer heights using remote sensing retrievals and ERA5 reanalysis over Central Amazonia. Remote Sens (Basel) 14, 4561.

Eresmaa, N., Karppinen, A., Joffre, S.M., Räsänen, J., Talvitie, H., 2006. Mixing height determination by ceilometer. Atmos Chem Phys 6, 1485–1493. https://doi.org/10.5194/ACP-6-1485-2006

Garratt, J.R., 1994. The atmospheric boundary layer. Earth Sci Rev 37, 89–134.

Govardhan, G., Nanjundiah, R.S., Satheesh, S.K., Krishnamoorthy, K., Kotamarthi, V.R., 2015. Performance of WRF-Chem over Indian region: Comparison with measurements. Journal of Earth System Science 124, 875–896.

Gunwani, P., Govardhan, G., Jena, C., Yadav, P., Kulkarni, S., Debnath, S., Pawar, P. V, Khare, M., Kaginalkar, A., Kumar, R., 2023. Sensitivity of WRF/Chem simulated PM2. 5 to initial/boundary conditions and planetary boundary layer parameterization schemes over the Indo-Gangetic Plain. Environ Monit Assess 195, 560.

Guo, J., Miao, Y., Zhang, Y., Liu, H., Li, Z., Zhang, W., He, J., Lou, M., Yan, Y., Bian, L., 2016. The climatology of planetary boundary layer height in China derived from radiosonde and reanalysis data. Atmos Chem Phys 16, 13309–13319.

Guo, P., Kuo, Y.H., Sokolovskiy, S. V., Lenschow, D.H., 2011. Estimating Atmospheric Boundary Layer Depth Using COSMIC Radio Occultation Data. J Atmos Sci 68, 1703–1713. https://doi.org/10.1175/2011JAS3612.1

Heffter J. L., 1980. Transport Layer Depth Calculations. Second Joint Conference on Applications of Air Pollution Meteorology, New Orleans, LA.

Hennemuth, B., Lammert, A., 2006. Determination of the atmospheric boundary layer height from radiosonde and lidar backscatter. Boundary Layer Meteorol 120, 181–200. https://doi.org/10.1007/S10546-005-9035-3/METRICS

Hersbach, H., Bell, B., Berrisford, P., Hirahara, S., Horányi, A., Muñoz-Sabater, J., Nicolas, J., Peubey, C., Radu, R., Schepers, D., Simmons, A., Soci, C., Abdalla, S., Abellan, X., Balsamo, G., Bechtold, P., Biavati, G., Bidlot, J., Bonavita, M., De Chiara, G., Dahlgren, P., Dee, D., Diamantakis, M., Dragani, R., Flemming, J., Forbes, R., Fuentes, M., Geer, A., Haimberger, L., Healy, S., Hogan, R.J., Hólm, E., Janisková, M., Keeley, S., Laloyaux, P., Lopez, P., Lupu, C., Radnoti, G., de Rosnay, P., Rozum, I., Vamborg, F., Villaume, S., Thépaut, J.N., 2020. The ERA5 global reanalysis. Quarterly Journal of the Royal Meteorological Society 146, 1999–2049. https://doi.org/10.1002/QJ.3803

Holtslag, A.A.M., Van Meijgaard, E., De Rooy, W.C., 1995. A comparison of boundary layer diffusion schemes in unstable conditions over land. Boundary Layer Meteorol 76, 69–95.

Jordan, N.S., Hoff, R.M., Bacmeister, J.T., 2010. Validation of Goddard Earth Observing System-version 5 MERRA planetary boundary layer heights using CALIPSO. Journal of Geophysical Research: Atmospheres 115.

Kalnay, E., Kanamitsu, M., Kistler, R., Collins, W., Deaven, D., Gandin, L., Iredell, M., Saha, S., White, G., Woollen, J., 2018. The NCEP/NCAR 40-year reanalysis project, in: Renewable Energy. Routledge, p. Vol1_146-Vol1_194.

Kanamitsu, M., Ebisuzaki, W., Woollen, J., Yang, S.-K., Hnilo, J.J., Fiorino, M., Potter, G.L., 2002. Ncep–doe amip-ii reanalysis (r-2). Bull Am Meteorol Soc 83, 1631–1644.

Kim, C.P., Entekhabi, D., 1998. Impact of soil heterogeneity in a mixed-layer model of the planetary boundary layer. Hydrological Sciences Journal 43, 633–658. https://doi.org/10.1080/02626669809492158

Kobayashi, S., Ota, Y., Harada, Y., Ebita, A., Moriya, M., Onoda, H., Onogi, K., Kamahori, H., Kobayashi, C., Endo, H., 2015. The JRA-55 reanalysis: General specifications and basic characteristics. Journal of the Meteorological Society of Japan. Ser. II 93, 5–48.

Kunhikrishnan, P.K., Gupta, K. Sen, JEEVA PRAKASH, J.W., Narayanan Nair, K., 1993. Study on thermal internal boundary layer structure over Thumba, India, in: Annales Geophysicae (1988). pp. 52–60.

Kursinski, E.R., Hajj, G.A., Schofield, J.T., Linfield, R.P., Hardy, K.R., 1997. Observing Earth's atmosphere with radio occultation measurements using the Global Positioning System. Journal of Geophysical Research: Atmospheres 102, 23429–23465.

Laloyaux, P., de Boisseson, E., Balmaseda, M., Bidlot, J., Broennimann, S., Buizza, R., Dalhgren, P., Dee, D., Haimberger, L., Hersbach, H., 2018. CERA-20C: A coupled reanalysis of the twentieth century. J Adv Model Earth Syst 10, 1172–1195.

Lavers, D.A., Beljaars, A., Richardson, D.S., Rodwell, M.J., Pappenberger, F., 2019. A forecast evaluation of planetary boundary layer height over the ocean. Journal of Geophysical Research: Atmospheres 124, 4975–4984.

Li, X., Dong, Y., Zhang, Y., Shi, Z., Yao, J., 2023. Climatology of planetary boundary layer height over Jiangsu, China, based on ERA5 reanalysis data. Atmosphere (Basel) 14, 1330.

Lieman, R., Alpert, P., 1993. Investigation of the planetary boundary layer height variations over complex terrain. Boundary Layer Meteorol 62, 129–142. https://doi.org/10.1007/BF00705550/METRICS

Min, J.S., Park, M.S., Chae, J.H., Kang, M., 2020. Integrated System for Atmospheric Boundary Layer Height Estimation (ISABLE) using a ceilometer and microwave radiometer. Atmos Meas Tech 13, 6965–6987. https://doi.org/10.5194/AMT-13-6965-2020

Moorthy, K.K., Beegum, S.N., Srivastava, N., Satheesh, S.K., Chin, M., Blond, N., Babu, S.S., Singh, S., 2013. Performance evaluation of chemistry transport models over India. Atmos Environ 71, 210–225.

Moorthy, K.K., Murthy, B.V.K., Nair, P.R., 1993. Sea-breeze front effects on boundary-layer aerosols at a tropical coastal station. J Appl Meteorol Climatol 32, 1196–1205.

Oke, T.R., 2002. Boundary layer climates. Routledge.

Pleim, J.E., Xiu, A., 1995. Development and testing of a surface flux and planetary boundary layer model for application in mesoscale models. Journal of Applied Meteorology (1988-2005) 16–32.

Puygrenier, V., Lohou, F., Campistron, B., Saïd, F., Pigeon, G., Bénech, B., Serça, D., 2005. Investigation on the fine structure of sea-breeze during ESCOMPTE experiment. Atmos Res 74, 329–353. https://doi.org/10.1016/J.ATMOSRES.2004.06.011

Qu, Y., Han, Y., Wu, Y., Gao, P., Wang, T., 2017. Study of PBLH and Its Correlation with Particulate Matter from One-Year Observation over Nanjing, Southeast China. Remote Sensing 2017, Vol. 9, Page 668 9, 668. https://doi.org/10.3390/RS9070668

Rani, S.I., Arulalan, T., George, J.P., Rajagopal, E.N., Renshaw, R., Maycock, A., Barker, D.M., Rajeevan, M., 2021. IMDAA: High-resolution satellite-era reanalysis for the Indian monsoon region. J Clim 34, 5109–5133.

Rani, S.I., Ramachandran, R., Subrahamanyam, D.B., Alappattu, D.P., Kunhikrishnan, P.K., 2010. Characterization of sea/land breeze circulation along the west coast of Indian sub-continent during pre-monsoon season. Atmos Res 95, 367–378. https://doi.org/10.1016/J.ATMOSRES.2009.10.009

Rienecker, M.M., Suarez, M.J., Gelaro, R., Todling, R., Bacmeister, J., Liu, E., Bosilovich, M.G., Schubert, S.D., Takacs, L., Kim, G.-K., 2011. MERRA: NASA's modern-era retrospective analysis for research and applications. J Clim 24, 3624–3648.

Russell, P.B., Uthe, E.E., Ludwig, F.L., Shaw, N.A., 1974. A comparison of atmospheric structure as observed with monostatic acoustic sounder and lidar techniques. J Geophys Res 79, 5555–5566.

Sathyanadh, A., Prabhakaran, T., Patil, C., Karipot, A., 2017. Planetary boundary layer height over the Indian subcontinent: Variability and controls with respect to monsoon. Atmos Res 195, 44–61.

Seibert, P., Beyrich, F., Gryning, S.-E., Joffre, S., Rasmussen, A., Tercier, P., 2000. Review and intercomparison of operational methods for the determination of the mixing height. Atmos Environ 34, 1001–1027.

Seidel, D.J., Zhang, Y., Beljaars, A., Golaz, J., Jacobson, A.R., Medeiros, B., 2012. Climatology of the planetary boundary layer over the continental United States and Europe. Journal of Geophysical Research: Atmospheres 117.

Shukla, K.K., Attada, R., Pathaikara, A., 2024. Climatology, trends, and variability of planetary boundary layer height over India using high-resolution Indian reanalysis. Theor Appl Climatol 155, 7937–7960.

Si, Y., Li, S., Chen, L., Yu, C., Wang, Z., Wang, Y., Wang, H., 2018. Validation and spatiotemporal distribution of GEOS-5–based planetary boundary layer height and relative humidity in China. Adv Atmos Sci 35, 479–492.

Singh, R., Ojha, S.P., Anthes, R., Hunt, D., 2021. Evaluation and assimilation of the COSMIC-2 radio occultation constellation observed atmospheric refractivity in the WRF data assimilation system. Journal of Geophysical Research: Atmospheres 126, e2021JD034935.

Slättberg, N., Lai, H., Chen, X., Ma, Y., Chen, D., 2022. Spatial and temporal patterns of planetary boundary layer height during 1979–2018 over the Tibetan Plateau using ERA5. International Journal of Climatology 42, 3360–3377.

Smith, E.K., Weintraub, S., 1953. The constants in the equation for atmospheric refractive index at radio frequencies. Proceedings of the IRE 41, 1035–1037.

Srinivas, C. V., Bhaskar Rao, D. V., Hari Prasad, D., Hari Prasad, K.B.R.R., Baskaran, R., Venkatraman, B., 2015. A Study on the Influence of the Land Surface Processes on the Southwest Monsoon Simulations

using a Regional Climate Model. Pure Appl Geophys 172, 2791–2811. https://doi.org/10.1007/S00024-014-0905-9/TABLES/2

Stull, R.B., 1988. An introduction to boundary layer meteorology. Springer Science & Business Media.

Van Ulden, A.P., Holtslag, A.A.M., 1985. Estimation of atmospheric boundary layer parameters for diffusion applications. Journal of Climate and Applied Meteorology 1196–1207.

Wang, Y., Gao, J., Mamtimin, A., Sayit, H., Zhou, C., Li, R., Dawut, M., Yang, F., Huo, W., Wen, C., 2023. Evolution law of atmospheric boundary layer in Gurbantünggüt Desert based on reanalysis dataset and in situ observation data. Heliyon 9.

Xi, X., Yang, Q., Liu, C., Shupe, M.D., Han, B., Peng, S., Zhou, S., Chen, D., 2024. Evaluation of the planetary boundary layer height from ERA5 reanalysis with MOSAiC observations over the Arctic Ocean. Journal of Geophysical Research: Atmospheres 129, e2024JD040779.

Xu, X., Luo, J., Shi, C., 2009. Comparison of COSMIC radio occultation refractivity profiles with radiosonde measurements. Adv Atmos Sci 26, 1137–1145. https://doi.org/10.1007/S00376-009-8066-Y/METRICS

Xu, Z., Chen, H., Guo, J., Zhang, G., Meng, C., Zhang, X., Hu, H., Miao, S., Zhai, P., 2023. Regionalization of the summertime planetary boundary layer height in comparison with various reanalysis datasets over China. Atmos Res 282, 106534.

Zhang, Y., Sun, K., Gao, Z., Pan, Z., Shook, M.A., Li, D., 2020. Diurnal climatology of planetary boundary layer height over the contiguous United States derived from AMDAR and reanalysis data. Journal of Geophysical Research: Atmospheres 125, e2020JD032803.

Zilitinkevich, S.S., Tyuryakov, S.A., Troitskaya, Y.I., Mareev, E.A., 2012. Theoretical models of the height of the atmospheric boundary layer and turbulent entrainment at its upper boundary. Izvestiya - Atmospheric and Ocean Physics 48, 133–142. https://doi.org/10.1134/S0001433812010148/METRICS

Supplementary Files

This is a list of supplementary files associated with this preprint. Click to download.

- SupplementaryABLHmanuscriptPS08012026.docx